Complexes of vertebrate TMC1/2 and CIB2/3 proteins form hair-cell mechanotransduction cation channels

Arnaud P. J. Giese[1,#,*], Wei-Hsiang Weng[2,3,*], Katie S. Kindt[4], Hui Ho Vanessa Chang[5], Jonathan S. Montgomery[2,6], Evan M. Ratzan[7], Alisha J. Beirl[4], Roberto Aponte Rivera[4], Jeffrey M. Lotthammer[2], Sanket Walujkar[2], Mark P. Foster[2,3,6], Omid A. Zobeiri[8], Jeffrey R. Holt[7], Saima Riazuddin[1], Kathleen E. Cullen[9], Marcos Sotomayor[2,3,6] , Zubair M. Ahmed[1,10,11]

[1]Department of Otorhinolaryngology – Head & Neck Surgery, University of Maryland School of Medicine, Baltimore, MD, USA.

[2]Department of Chemistry and Biochemistry, The Ohio State University, Columbus, OH, USA.

[3]Biophysics Graduate Program, The Ohio State University, Columbus, OH, USA.

[4]Section on Sensory Cell Development and Function, National Institute on Deafness and Other Communication Disorders, National Institutes of Health, Bethesda, MD, USA.

[5]Department of Physiology, McGill University, Montreal, QC, Canada.

[6]Ohio State Biochemistry Program, The Ohio State University, Columbus, OH, USA.

[7]Departments of Otolaryngology and Neurology, F.M. Kirby Neurobiology Center, Boston Children's Hospital, Harvard Medical School, Boston, MA, USA.

[8]Department of Biomedical Engineering, McGill University, Montreal, QC, Canada.

[9]Departments of Biomedical Engineering, Neuroscience, and Otolaryngology and Head and Neck Surgery, Johns Hopkins University School of Medicine, Baltimore, MD, USA.

22 [10]Department of Biochemistry and Molecular Biology, University of Maryland School of
23 Medicine, Baltimore, MD, USA.
24 [11]Department of Ophthalmology and Visual Sciences, University of Maryland School of
25 Medicine, Baltimore, MD, USA.
26 [#]Current address: SENSORION SA, Montpellier, France.
27 *Contributed equally.
28 Correspondance:
29 Emails: sotomayor@uchicago.edu; zmahmed@som.umaryland.edu
30
31 Keywords: CIB2, CIB3, mechanotransduction, TMC1, TMC2, Vestibular hair cells

Abstract

Calcium and integrin-binding protein 2 (CIB2) and CIB3 bind to transmembrane channel-like 1 (TMC1) and TMC2, the pore-forming subunits of the inner-ear mechano-electrical transduction (MET) apparatus. These interactions have been proposed to be functionally relevant across mechanosensory organs and vertebrate species. Here we show that both CIB2 and CIB3 can form heteromeric complexes with TMC1 and TMC2 and are integral for MET function in mouse cochlea and vestibular end organs as well as in zebrafish inner ear and lateral line. Our AlphaFold 2 models suggest that vertebrate CIB proteins can simultaneously interact with at least two cytoplasmic domains of TMC1 and TMC2 as validated using nuclear magnetic resonance spectroscopy of TMC1 fragments interacting with CIB2 and CIB3. Molecular dynamics simulations of TMC1/2 complexes with CIB2/3 predict that TMCs are structurally stabilized by CIB proteins to form cation channels. Overall, our work demonstrates that intact CIB2/3 and TMC1/2 complexes are integral to hair-cell MET function in vertebrate mechanosensory epithelia.

46 **Introduction**

47 The vertebrate senses of hearing and balance depend on the process of mechano-electrical
48 transduction (MET) in inner-ear hair cells. This process is initiated when mechanical forces from
49 sound waves and head movements deflect specialized mechanosensory projections at the apical
50 surface of hair cells, known as stereocilia (reviewed in Fettiplace, 2017; Frolenkov et al., 2004;
51 Gillespie and Müller, 2009). Deflections of stereocilia result in tensioning of the extracellular tip
52 links that convey mechanical force to the MET channels. Mature tip links are heterotetrameric
53 filaments composed of cadherin 23 (CDH23) and protocadherin 15 (PCDH15) (Ahmed et al.,
54 2006; Kazmierczak et al., 2007; Siemens et al., 2004; Söllner et al., 2004; Sotomayor et al., 2012).
55 In mammalian auditory hair cells, MET channels are localized at the PCDH15 end of the tip link
56 (Beurg et al., 2009). Significant progress in our understanding of MET has been recently made by
57 identifying the transmembrane channel-like proteins 1 and 2 (TMC1 and TMC2) as the pore-
58 forming subunits of the MET channel (Kawashima et al., 2011; Pan et al., 2018). In hair cells, two
59 other transmembrane proteins, LHFPL5 and TMIE, are essential for sustained hearing. LHFPL5
60 binds to PCDH15 and may regulate force transmission to TMC1 and TMC2 (Qiu et al., 2023;
61 Xiong et al., 2012). TMIE also interacts with TMC1/2 and regulates unitary conductance and ion
62 selectivity of the MET channels (Cunningham et al., 2020; Naz et al., 2002). Interestingly, MET
63 currents can still be recorded from hair cells lacking LHFPL5 or TMIE, suggesting that neither are
64 essential for channel function (Fettiplace et al., 2022), yet all are needed for sustained hair-cell
65 transduction and normal hearing. In zebrafish, Tmcs, Lhfpl5, Tmie, and Pcdh15 are also essential
66 for sensory transduction, suggesting that these molecules form the core MET complex in all
67 vertebrate hair cells (Chen et al., 2020; Erickson et al., 2019, 2017; Ernest et al., 2000; Gleason et
68 al., 2009; Gopal et al., 2015; Maeda et al., 2017, 2014; Pacentine and Nicolson, 2019; Phillips et

69 al., 2011; Seiler et al., 2004; Söllner et al., 2004).

70 We previously showed that calcium (Ca^{2+}) and integrin-binding protein 2 (CIB2), and the
71 closely related CIB3, interact with TMC1/2 (Giese et al., 2017). Furthermore, we also
72 demonstrated that CIB2 is essential for MET function in auditory hair cells (Giese et al., 2017).
73 Recessive variants of *CIB2* predominantly cause nonsyndromic DFNB48 hearing loss in humans
74 (Booth et al., 2018; Michel et al., 2017; Riazuddin et al., 2012; Seco et al., 2016; Wang et al.,
75 2017). Similarly, recessive alleles of *Cib2* cause hearing loss in mice but no vestibular deficits
76 (Giese et al., 2017; Michel et al., 2017; Wang et al., 2017). In zebrafish, knockdown of *Cib2*
77 diminishes both the acoustic startle response and mechanosensitive responses of lateral-line hair
78 cells (Riazuddin et al., 2012). CIB2 belongs to a family of four closely related proteins (CIB1-4)
79 that have partial functional redundancy and similar structural domains, with at least two
80 Ca^{2+}/Mg^{2+}-binding EF-hand motifs that are highly conserved for CIB2/3 (Huang et al., 2012).
81 Wang and co-authors investigated the function of *Cib1* in cochlear hair cells through generation
82 of a knockout strain and concluded that although *Cib1* is expressed in the mouse cochlear hair
83 cells, loss of CIB1 protein did not affect auditory function (Wang et al., 2017). A recent study
84 demonstrated that while CIB2 is essential for proper localization of TMC1/2 at the tips of auditory
85 hair cell stereocilia, CIB3 can restore MET currents in cochlear hair cells lacking CIB2 (Liang et
86 al., 2021). The same study reported a crystal structure of a TMC1 intracellular linker in complex
87 with CIB3, which suggests that CIB2/3 proteins are likely to be auxiliary subunits of hair cell MET
88 channels (Liang et al., 2021).

89 Previous work on CIB proteins primarily focused on auditory hair cells, leaving open the
90 question of whether they play a role in vestibular function. This question was addressed in part by

91 another recent study that reported vestibular deficits in mice lacking both CIB2 and CIB3 (Wang
92 et al., 2023). However, additional evidence showing that CIB2/3 can function and interact with
93 TMC1/2 proteins across sensory organs, hair-cell types, and species is still needed. Here we
94 provide further evidence that CIB2 and CIB3 are indeed evolutionary conserved and functionally
95 redundant components of the vertebrate transduction apparatus necessary for MET channel activity
96 in mouse vestibular hair cells, as well as in zebrafish mechanosensory epithelia. Moreover, based
97 on our structural analyses and simulations, we propose that CIB2 and CIB3 are required for
98 stabilization and channel function of the MET proteins TMC1 and TMC2.

99

100 **Results**

101 **CIB2 and CIB3 are expressed in mouse vestibular hair cells**

102 We and others previously demonstrated that CIB2 is essential for MET in auditory hair
103 cells (Giese et al., 2017; Michel et al., 2017; Wang et al., 2017). In contrast to auditory hair cells,
104 we found that the vestibular hair cells in *Cib2*$^{KO/KO}$ mice apparently have MET. We assessed MET
105 via uptake of FM 1-43 (Figure 1A), a styryl dye that mostly permeates into hair cells through
106 functional MET channels (Meyers et al., 2003), indicating that there may be another CIB protein
107 playing a functionally redundant role. Bulk RNA sequencing revealed that all four members of the
108 *Cib* family are expressed in mouse inner ear tissues (Figure 1B). However, when assessed by single
109 cell RNA sequencing analysis, only *Cib2* and *Cib3* are expressed in immature hair cells in the
110 mouse utricle (Figure 1C), a vestibular sensory organ required to detect linear acceleration
111 (McInturff et al., 2018). Further, we find that the expression of *Cib2* and *Cib3* is maintained in
112 mature type 1 and type 2 utricular hair cells (Figure 1C). We also examined the expression of *Tmc1*

113 and *Tmc2* in utricular hair cells and found that in immature hair cells *Tmc1* is highly expressed,
114 while *Tmc2* expression is low (Figure 1C). *Tmc2* expression increases during development but
115 remains below *Tmc1* levels in both type 1 and type 2 hair cells upon maturation (Figure 1C). CIB2
116 and CIB3 have been reported to interact with TMC1/2, and CIB2 is essential for auditory hair cell
117 MET (Giese et al., 2017; Liang et al., 2021). The co-expression of *Cib2* and *Cib3* in developing
118 and mature vestibular hair bundles, and the ability of CIB2/3 to interact with TMC1 and TMC2,
119 all make them attractive candidates to regulate MET function in vestibular hair cells.

120

121 **CIB3 is not required for hearing function in mice**

122 To evaluate whether CIB3 regulates MET function both in auditory and vestibular hair
123 cells, we generated *Cib3* knockout ($Cib3^{KO}$) mice using CRISPR/Cas9 technology (Figure 1D).
124 An indel in exon 4 of *Cib3* was introduced leading to a nonsense mutation (p.Asp54*), thus causing
125 a loss of allele function (Figure 1E-F). We first characterized hearing function in $Cib3^{KO/KO}$ and
126 control littermate mice at P16 by measuring auditory-evoked brainstem responses (ABRs). Normal
127 ABR waveforms and thresholds were observed in $Cib3^{KO/KO}$ indicating normal hearing. Next, we
128 investigated if there was a functional redundancy between CIB2 and CIB3 in auditory hair cells.
129 For this analysis, the $Cib3^{KO}$ allele was introduced into the $Cib2^{KO}$ background. Similar to what
130 has been previously reported in $Cib2^{KO/KO}$ mice (Giese et al., 2017; Michel et al., 2017; Wang et
131 al., 2017), the *Cib2:Cib3* double knockout ($Cib2^{KO/KO};Cib3^{KO/KO}$) mice were also profoundly deaf.
132 The $Cib2^{KO/KO};Cib3^{KO/KO}$ mice did not respond to click or strong tone burst stimuli at 100 dB sound
133 pressure level (SPL) (Figure 2A-B). As reported previously for $Cib2^{KO/KO}$ mice, we observed that
134 auditory hair cells in $Cib2^{KO/KO};Cib3^{KO/KO}$ mice did not accumulate FM 1-43 dye (Figure 2C).

135 Also, similar to *Cib2*$^{KO/KO}$ mice (Giese et al., 2017; Michel et al., 2017; Wang et al., 2017), we
136 observed progressive degeneration of auditory hair cells in *Cib2*$^{KO/KO}$*;Cib3*$^{KO/KO}$ mice (Figure 2D).
137 Taken together with previous studies, our results confirm that CIB2 is indispensable for hearing
138 and MET function in the auditory hair cells.

139

140 **CIB2 and CIB3 are required for vestibular function in mice**

141 After we assessed auditory function, we turned our analyses toward vestibular function.
142 Similar to *Cib2*$^{KO/KO}$ mice (Giese et al., 2017), *Cib3*$^{KO/KO}$ mice did not display any obvious
143 indications of vestibular dysfunction, such as circling, hyperactivity or head bobbing, performed
144 well when exploratory behavior was tested, and had normal vestibulo-ocular reflexes (Figure 3).
145 In contrast, visual observation of the *Cib2*$^{KO/KO}$*;Cib3*$^{KO/KO}$ mice indicated altered exploratory
146 behavior in an open-field test, suggesting an impairment of the vestibular system (Figure 3A-B).
147 To assess the implications of the *Cib2*$^{KO/KO}$*;Cib3*$^{KO/KO}$ mice on vestibular function, we next
148 performed a series of tests, including: the vestibulo-ocular reflex (VOR), performance in a rotating
149 rod, and head movement analysis (Figure 3C-H). The VOR is mediated by a direct three neuron
150 pathway linking the vestibular nerve to the extraocular muscles and produces compensatory eye
151 movements in the direction opposite of the head movement to provide stable gaze (reviewed in
152 Cullen, 2019). The dynamic response properties (i.e., gain and phase) of the VOR can be precisely
153 quantified in response to rotations applied at different frequencies in darkness (VORd). In response
154 to VORd testing, *Cib2*$^{+/+}$*;Cib3*$^{KO/KO}$ mice generated robust compensatory eye movements (Figure
155 3C, black trace). In contrast, *Cib2*$^{KO/KO}$*;Cib3*$^{KO/KO}$ mice generated negligible eye movements
156 (Figure 3C, red trace). Consistent with this observation, quantification of the VORd across

157 frequencies (Figure 3D) revealed gains near zero in the *Cib2*$^{KO/KO}$;*Cib3*$^{KO/KO}$ mice that were
158 significantly reduced (p<0.05) compared to those measured in *Cib2*$^{+/+}$;*Cib3*$^{KO/KO}$ mice.
159 Interestingly, the VORd gains of *Cib2*$^{KO/+}$;*Cib3*$^{KO/KO}$ mice also showed attenuation with a
160 significant decrease at 2 Hz (p<0.01) compared to *Cib2*$^{+/+}$;*Cib3*$^{KO/KO}$ mice. On the other hand, the
161 response phase of VORd eye movements were comparable for *Cib2*$^{KO/+}$;*Cib3*$^{KO/KO}$ and *Cib2*$^{+/+}$;
162 *Cib3*$^{KO/KO}$ mice at all frequencies (p>0.05) (Figure 3D).

163 As a control for possible changes in visual system and/or ocular motor pathway, we also
164 quantified the optokinetic reflex (OKR), which generates eye movements in responses to a moving
165 visual scene and in light. The OKR normally works together with the VOR to stabilize the visual
166 field on the retina. Both *Cib2*$^{+/+}$;*Cib3*$^{KO/KO}$ and *Cib2*$^{KO/+}$;*Cib3*$^{KO/KO}$ showed robust OKN responses
167 which similarly decreased as a function of frequency (Figure 3E; p>0.05). Likewise, OKR gain
168 values in *Cib2*$^{KO/KO}$;*Cib3*$^{KO/KO}$ were comparable with the single exception of a significant gain
169 decrease at 0.2 Hz (p<0.05). Analysis of OKN similarly revealed comparable response phase for
170 all 3 groups of mice at all frequencies (p>0.05) with the exception that the *Cib2*$^{KO/KO}$;*Cib3*$^{KO/KO}$
171 mice demonstrated less lag at 0.8 and 2 Hz (Figure 3E-F). Overall, the OKR responses of mutant
172 and control mice were generally comparable.

173 In addition to generating compensatory VOR eye movements to stabilize gaze, the
174 vestibular system also plays a key role in the maintenance of posture and control of balance. Thus,
175 we also tested all 3 groups of mice on several vestibular tasks that assessed balance and postural
176 defects. First, quantification of open-field testing experiments confirmed that mice exhibited
177 circling – a behavior that is commonly associated with loss of vestibular function in mice (Figure
178 3B; p<0.002). We also completed rotarod testing in which performance was quantified by

179 measuring the amount of time the mouse remained on the rotating rod as its acceleration increased.
180 While *Cib2*$^{+/+}$;*Cib3*$^{KO/KO}$ and *Cib2*$^{KO/+}$;*Cib3*$^{KO/KO}$ mice exhibited similar performance,
181 *Cib2*$^{KO/KO}$;*Cib3*$^{KO/KO}$ mice exhibited significantly poorer performance across all time points from
182 day 1 through day 4 (Figure 3G, $p<0.002$). Finally, it was also possible to distinguish
183 *Cib2*$^{KO/KO}$;*Cib3*$^{KO/KO}$ mice from the other two groups in their home cages since they commonly
184 displayed head bobbing, a trait also generally associated with vestibular dysfunction in mice. To
185 quantify head movement in our mice, we attached a 6D MEMS module consisting of three
186 gyroscopes and three linear accelerometers to the mouse's head implant (see Methods). Analysis
187 of power spectra of head motion revealed significantly higher power for *Cib2*$^{KO/KO}$;*Cib3*$^{KO/KO}$ mice
188 in all six dimensions of motion, as compared to *Cib2*$^{KO/+}$;*Cib3*$^{KO/KO}$ and *Cib2*$^{+/+}$;*Cib3*$^{KO/KO}$ mice
189 (Figure 3H, compare red vs. blue and black). Further, there were no significant differences in the
190 head movements power spectra of *Cib2*$^{KO/+}$;*Cib3*$^{KO/KO}$ and *Cib2*$^{+/+}$;*Cib3*$^{KO/KO}$ mice (Figure 3H,
191 blue vs. black). Taken together our findings indicate that *Cib2*$^{KO/KO}$;*Cib3*$^{KO/KO}$ mice show marked
192 deficits in vestibulomotor function when compared to both *Cib2*$^{KO/+}$;*Cib3*$^{KO/KO}$ and
193 *Cib2*$^{+/+}$;*Cib3*$^{KO/KO}$ mice.

194

195 **CIB2 and CIB3 are functional subunits of the MET apparatus in mouse vestibular hair cells**

196 To understand the root cause of vestibulomotor function deficits described above for
197 *Cib2*$^{KO/KO}$;*Cib3*$^{KO/KO}$ mice, we first analyzed vestibular hair bundle morphology using confocal
198 microscopy. High-resolution confocal imaging did not reveal any obvious vestibular hair cell loss
199 in *Cib2*$^{KO/KO}$;*Cib3*$^{KO/KO}$ mice (Figure 4A). Next, we visualized MET activity in vestibular hair cells
200 of saccular and utricular end organs of *Cib2*$^{KO/KO}$;*Cib3*$^{KO/KO}$ mice using the styryl dye FM 1-43.

201 These vestibular end organs are divided into two main physically and functionally distinct
202 domains, a central striolar domain and a peripheral extrastriolar domain. At P5, FM 1-43 labeling
203 of *Cib2*$^{KO/KO}$; *Cib3*$^{KO/KO}$ tissue failed to label vestibular hair cells in appreciable numbers (Figure
204 4B). Similarly, fixable FM 1-43FX intraperitoneal injections at P60 also showed no dye uptake in
205 *Cib2*$^{KO/KO}$; *Cib3*$^{KO/KO}$ mice (Figure 4C). *Cib2*$^{KO/KO}$ and *Cib3*$^{KO/KO}$ single mutant mice had dye
206 uptake both in striolar and extrastriolar hair cells, although a subtle reduction in FM 1-43FX was
207 observed in extrastriolar hair cells of both single mutants at P60 (Figure 4C). Taken together, these
208 results support compulsory but functionally redundant roles for CIB2 and CIB3 in the vestibular
209 hair cell MET complex.

210

211 **Cib2 and Cib3 function is evolutionary conserved in zebrafish**

212 Numerous studies have shown that the same proteins are required for hair cell MET in
213 zebrafish and mammals (Chen et al., 2020; Erickson et al., 2017; Ernest et al., 2000; Gleason et
214 al., 2009; Gopal et al., 2015; Maeda et al., 2017, 2014; Phillips et al., 2011; Seiler et al., 2004;
215 Söllner et al., 2004). Unlike mammals, the zebrafish inner ear does not have a cochlea. Instead,
216 zebrafish rely on their saccule for hearing and utricle for balance. Zebrafish also utilize hair cells
217 in a specialized sensory system, the lateral line, to detect local water movement. The hair cells
218 within both the zebrafish inner ear and lateral line share many morphologically similarities to
219 mammalian vestibular hair cells (Nicolson, 2017). Zebrafish scRNAseq data show that both *cib2*
220 and *cib3* are expressed in inner ear while primarily *cib2* is expressed in lateral-line hair cells (Baek
221 et al., 2022; Shi et al., 2023). Given the zebrafish reliance on the saccule for hearing and the

222 similarities between zebrafish hair cells to mammalian vestibular hair cells, we tested whether
223 Cib2 and/or Cib3 were required for hair cell MET in the zebrafish inner ear or lateral line.
224 To examine the impact of Cib2 and Cib3 loss in zebrafish, we created mutants using
225 CRISPR-Cas9 based methods to target each homologue (Varshney et al., 2016). Both mutants lead
226 to a stop codon in the last EF-hand domain (Figure 5-figure supplement 1). We first examined
227 auditory function by testing the acoustic startle reflex in *cib2* and *cib3* mutants. For our
228 experiments we used a Zantiks behavioral system to quantify the probability of generating a startle
229 in response to a vibrational tap stimulus. This response is thought to rely primarily on hair cells in
230 the zebrafish saccule and lateral-line system. We found that, compared to controls, the probability
231 of a startle response was significantly reduced in *cib2* mutants (Figure 5A, control: 0.71 ± 0.04;
232 *cib2*: 0.28 ± 0.06, $p = 0.005$). In contrast, *cib3* mutants startle with a similar frequency compared
233 to controls (Figure 5A, $p = 0.36$). Interestingly, contrary to mammals, where CIB2 is crucial for
234 hearing, acoustic startle responses were not completely eliminated in *cib2* mutants. One possibility
235 for this partial loss of acoustic startle is that Cib3 may be able to compensate for Cib2 in the
236 zebrafish. Therefore, we examined acoustic startle responses in *cib2;cib3* mutants. In *cib2;cib3*
237 mutant animals we observed a complete absence of startle responses (Figure 5A). Furthermore,
238 we observed that *cib2;cib3* mutants but not *cib2* or *cib3* mutants exhibited spontaneous circling
239 behavior, an additional indicator of inner ear dysfunction in zebrafish (Nicolson et al., 1998).
240 Together our behavioral results indicate that Cib2 and Cib3 are both required to ensure normal
241 acoustic startle responses in zebrafish. Furthermore, just loss of Cib2, but not Cib3 can impair
242 auditory function in zebrafish.
243
244 **Cib2 and Cib3 are required for MET in the zebrafish lateral line**

245 Our results demonstrate that both Cib2 and Cib3 are required for proper auditory function
246 in zebrafish. This raises the question of whether, similar to mice, these proteins are critical for
247 MET function in zebrafish hair cells. Therefore, we next turned our analysis to hair cells in
248 neuromast organs of the lateral line where methods to assess MET are well-documented and
249 straightforward (Lukasz and Kindt, 2018; Seiler et al., 2004).

250 First, to assess whether there were gross alterations to MET in lateral-line hair cells we
251 examined uptake of the FM 1-43. We found that, compared to controls, the percent of hair cells
252 per neuromast labeling with FM 1-43 was significantly reduced in *cib2* mutants (Figure 5B,D,E,
253 control: 97.6 ± 1.2; *cib2*: 37.5 ± 6.9, $p < 0.0001$). In contrast, a similar percent of hair cells per
254 neuromast labeled with FM 1-43 in *cib3* mutants, compared to controls (Figure 5B,D,F, *cib3*: 95.7
255 ± 1.9, $p = 1.0$). We also quantified the average intensity of the FM 1-43 in hair cells (Figure 5C).
256 We found that, compared to controls, the average FM 1-43 label was reduced in *cib2* but not *cib3*
257 mutants (Figure 5C). In *cib2* mutants we did observe residual hair cells that labeled with FM 1-43.
258 We hypothesized that in lateral-line hair cells, similar to its role in zebrafish auditory function,
259 Cib3 may be able to substitute for Cib2 in MET. To assess whether Cib3 can substitute for Cib2,
260 we examined FM 1-43 labeling in *cib2;cib3* mutants. In *cib2;cib3* mutant animals we observed a
261 complete absence of FM 1-43 labeling in lateral-line hair cells (Figure 5B,D,G). Thus, taken
262 together the results of our FM 1-43 labeling analysis are consistent with a requirement for both
263 Cib2 and Cib3 to ensure normal MET in all lateral-line hair cells.

264 To obtain a more quantitative assessment of MET we used Ca^{2+} imaging to perform evoked
265 measurements of hair cell function. For this assessment, we used a transgenic line that expresses a
266 membrane-localized GCaMP6s (memGCaMP6s) specifically in hair cells (Figure 5H-I'). This
267 transgenic line has previously been used to measure Ca^{2+} influx into apical hair bundles while

268 stimulating lateral-line hair cells with a fluid-jet (Figure 5H-I') (Lukasz and Kindt, 2018). Using
269 this approach, we were able to stimulate and monitor stimulus-evoked mechanosensitive Ca^{2+}
270 responses in hair bundles within neuromast organs of each genotype (Representative responses:
271 Figure 5I-L). We quantified the number of hair bundles per neuromast with mechanosensitive Ca^{2+}
272 responses, and found that compared to controls, significantly fewer cells were mechanosensitive
273 in *cib2* and *cib2*;*cib3* mutants (Figure 5-figure supplement 2A, control: 92.2 ± 2.5; *cib2*: 49.9 ±
274 5.8, *cib2;cib3:* 19.0 ± 6.6, $p > 0.0001$). In contrast, in *cib3* mutants, the percent of
275 mechanosensitive cells per neuromast was similar compared to controls (Figure 5-figure
276 supplement 2A, *cib3*: 94.5 ± 1.8, $p = 1.0$). We also quantified the magnitude of the
277 mechanosensitive Ca^{2+} signal in the hair bundles, focusing on only the responsive hair cells for
278 each genotype. This quantification revealed that, while *cib3* mechanosensitive responses were not
279 different compared to controls (Figure 5-figure supplement 2B-C, GCaMP6s % $\Delta F/F$ control: 70.6
280 ± 5.9; *cib3*: 71.6 ± 5.2, $p > 1.0$), the magnitude of responses in *cib2* and *cib2*;*cib3* hair bundles was
281 significantly reduced (Figure 5-figure supplement 2B-C, GCaMP6s % $\Delta F/F$ control: 70.6 ± 5.9;
282 *cib2*: 33.0 ± 5.8, *cib2;cib3:* 14.7 ± 1.9, $p < 0.0001$). Overall, our *in vivo* FM 1-43 and Ca^{2+}-imaging
283 analyses revealed that loss of Cib2 alone, but not Cib3 can impair mechanosensory function in the
284 majority of zebrafish lateral-line hair cells. Furthermore, Cib2 and Cib3 are both required to ensure
285 normal MET function in all lateral-line hair cells.
286
287 **Cib2 is required in specific subsets of hair cells in the zebrafish lateral line and inner ear**
288 Previous work has shown that within the zebrafish inner ear and lateral line there are
289 distinct hair cell subtypes that rely on different complements of the mechanosensitive ion channel
290 Tmc: Tmc1, 2a and 2b. In the primary posterior lateral line (pLL) hair cells are oriented to respond

291 to either anterior or posterior fluid flow. The subset of hair cells that detects posterior flow relies
292 on Tmc2b while the subset that detects anterior flow relies on both Tmc2b and Tmc2a (Figure 6A)
293 (Chou et al., 2017). Further, work with the crista of the zebrafish inner ear has shown that there
294 are two morphologically distinct types of hair cells: short, teardrop-shaped cells with taller hair
295 bundles and tall, gourd-shaped cells with shorter hair bundles (Smith et al., 2020; Zhu et al., 2021).
296 Short cells rely on Tmc2a, while tall cells rely on either Tmc1 or Tmc2b for mechanosensitive
297 function (Figure 6E) (Smith et al., 2020). Based on this work, we hypothesized that Cib2 or Cib3
298 could have specific roles in zebrafish hair cell sensory organs linked to hair cell orientation in the
299 lateral line or morphology type in the crista of the inner ear.

300 Our FM 1-43 labeling in neuromasts revealed no defect in *cib3* mutants, suggesting that
301 Cib2 can compensate for Cib3 in all pLL hair cells. In contrast to *cib3* mutants, only a subset of
302 hair cells per neuromast were labeled with FM 1-43 in *cib2* mutants (Figure 5E). Previous work
303 has shown that in the pLL of *tmc2b* mutants, a subset of hair cells that respond to anterior flow
304 label with FM 1-43 (Chou et al., 2017). This residual FM 1-43 label is dependent on Tmc2a.
305 Therefore, we examined whether the remaining, FM 1-43 positive hair cells in *cib2* mutants have
306 a specific hair cell orientation. For this analysis, we used a fixable form of FM 1-43, FM 1-43FX
307 to label hair cells. After FM 1-43FX labeling, we fixed the larvae and labeled the apical hair
308 bundles with phalloidin to reveal hair cell orientation. This analysis revealed that in sibling
309 controls, a similar percentage of FM 1-43FX positive hair cells are oriented to respond to anterior
310 and posterior flow (Figure 6B,B',D). In contrast, when we examined *cib2* mutants, we found that
311 significantly more of the FM 1-43 positive hair cells were oriented to respond to posterior flow
312 (Figure 6C-D). This indicates that in *cib2* mutants, the residual Cib3 present in pLL hair cells
313 preferentially functions in hair cells that express primarily Tmc2b and are oriented to respond to

314 posterior flow (Figure 6A). On the other hand, Cib2 can function with hair cells that express Tmc2b
315 (respond to posterior flow) as well as hair cells that express Tmc2b and Tmc2a (respond to anterior
316 flow).

317 Next, we examined whether different hair-cell subtypes (short versus tall morphology) in
318 the zebrafish inner ear preferentially rely on Cib2 or Cib3 for mechanosensitive function. To
319 examine MET function, we injected FM 4-64 into the zebrafish ear in a transgenic background
320 that labels the hair cell membrane (memGCaMP6s). FM 4-64 is a redshifted version of FM 1-43
321 and provides a similar readout of MET (Erickson et al., 2017; Smith et al., 2020). After injection,
322 we imaged FM 4-64 label in the medial cristae, an inner ear sensory organ that allows for excellent
323 delineation of short and tall cell types (Figure 6F-F'). We found that similar to our FM 1-43 results
324 in the pLL, no hair cells in the medial cristae were FM 4-64 positive in *cib2;cib3* double mutants
325 (Figure 6I-I'). In addition, similar to the pLL we observed no defects in FM 4-64 labeling in the
326 crista of *cib3* mutants compared to controls (Figure 6G-G'). Interestingly we found that short hair
327 cells in the crista of *cib2* mutants failed to label with FM 4-64 (Figure 6H-H'). Previous work has
328 shown that short hair cells rely on Tmc2a for mechanosensitive function (Smith et al., 2020).
329 Overall, our functional assessment of MET based on hair cell subtypes within the zebrafish pLL
330 and inner ear suggests that Cib2 is required for mechanosensitive function in hair cells that express
331 Tmc2a.

332

333 **CIB proteins simultaneously interact with at least two cytoplasmic domains of TMC1**

334 To gain molecular insight into the role played by CIB proteins in hair-cell MET, we
335 generated AlphaFold 2 (AF2) (Jumper et al., 2021; Tunyasuvunakool et al., 2021) models of the
336 human TMC1 dimer, alone and in complex with human CIB2/3 (Figure 7A-B; Figure 7-figure

337 supplement 1; Figure 7-video 1). The AF2 model of TMC1 alone resembles previous
338 TMEM16/OSCA-based models of TMC1 and is also consistent with a recent cryo-EM structure
339 of the worm TMC-1 protein (Ballesteros et al., 2018; Jeong et al., 2022; Pan et al., 2018; Walujkar
340 et al., 2021). In these models, TMC1 has ten transmembrane domains (α1 to α10; Figure 7-figure
341 supplements 1-2) and a putative pore is formed by transmembrane helices α4, α5, α6, and α7 at
342 the periphery of each monomer (Pan et al., 2018; Walujkar et al., 2021), away from the dimeric
343 interface involving α10. Our new models feature an additional amphipathic helix, which we denote
344 α0, extending almost parallel to the expected plane of the membrane bilayer without crossing
345 towards the extracellular side (as observed for a mostly hydrophobic α0 in OSCA channels and
346 labeled as H3 in the worm TMC-1 structure) (Jeong et al., 2022; Jojoa-Cruz et al., 2018; Liu et al.,
347 2018; M. Zhang et al., 2018). Extracellular and intracellular domains linking transmembrane
348 helices, which were either omitted or poorly predicted in previous work (Ballesteros et al., 2018;
349 Pan et al., 2018; Walujkar et al., 2021), have well-defined secondary structure and a high
350 confidence score (pLDDT > 70 for most regions; Figure 7-figure supplement 1A). The intracellular
351 domain linking helices α2 and α3, denoted here as IL1, adopts a helix-loop-helix with the two
352 helices running parallel to each other and differing in length (Figure 7-figure supplements 1-5).
353 This is the same fold observed in its crystal structure in complex with CIB3 (Liang et al., 2021),
354 which validated the modeling approach.

355 Interestingly, AF2 models of TMC1 in complex with CIB2 suggest that the N-terminus
356 (NT) of TMC1 also interacts with CIB2 (Figure 7A-B). In our model, CIB2 is clamped between
357 TMC1-NT and TMC1-IL1 while the first helix of TMC1-IL1 runs parallel to the membrane plane
358 interacting with the base of α1 and the intracellular linkers between α4 and α5, α6 and α7, and

359 α8 and α9. Notably, the predicted interaction between TMC1-NT and CIB2 is consistent with
360 previous biochemical data (Giese et al., 2017), while the overall model resolves seemingly
361 contradictory results indicating that either the NT or IL1 of TMC1 were responsible for
362 interactions with CIB proteins (Giese et al., 2017; Liang et al., 2021). Additional AF2 models of
363 TMC1 with CIB3 and of TMC2 with CIB2/3 (Figure 7-figure supplement 1) predicted the same
364 architecture for the TMC1/2 + CIB2/3 complexes where CIB proteins are clamped between the
365 IL1 and NT domains of TMCs. Predictions for fish complexes also show the same general
366 architecture (Figure 7-figure supplement 1A).

367 Nuclear magnetic resonance (NMR) experiments were used to validate the clamp model
368 for *Homo sapiens* (*hs*) TMC + CIB interactions. We produced uniformly ^{15}N labeled *hs* CIB2 (22.7
369 kDa) and CIB3 (22.9 kDa) proteins ([U-^{15}N]-*hs* CIB2/3), alone or co-refolded with unlabeled *hs*
370 TMC1-IL1 (6.3 kDa). In parallel, we produced an unlabeled soluble TMC1-NT fragment (6.9 kDa)
371 and used these CIB and TMC1 samples to test protein-protein interactions by monitoring their
372 effects on 2D ^{1}H-^{15}N-correlation spectra of the labeled CIB2 and CIB3 proteins. All protein
373 fragments were purified using size exclusion chromatography (SEC) (Figure 7-figure supplement
374 6), revealing a single monodisperse peak for [U-^{15}N]-*hs* CIB2 (69.2 mL elution volume in S75
375 16/600 column) and a slightly displaced peak for [U-^{15}N]-*hs* CIB2 + *hs* TMC1-IL1 (68.5 mL). In
376 contrast, SEC experiments revealed two peaks for [U-^{15}N]-*hs* CIB3 alone (potential dimer at 62.8
377 mL and potential monomer at 73.1 mL) and a single peak for [U-^{15}N]-*hs* CIB3 + *hs* TMC1-IL1
378 (71.3 mL). ^{1}H-^{15}N-correlation spectra of [U-^{15}N]-*hs* CIB2 alone were consistent with prior data
379 indicating that many, but not all potential peaks are resolved (Figure 7C, Figure 7-figure
380 supplement 7A) (Huang et al., 2012). Spectra for the [U-^{15}N]-*hs* CIB2 + *hs* TMC1-IL1 complex
381 exhibit widespread perturbations, consistent with extensive remodeling of the CIB2 structure.

382 Moreover, addition of *hs* TMC1-NT induced additional chemical shift perturbations in many, but
383 not all peaks, demonstrating that the TMC1-IL1 and TMC1-NT ligands bind simultaneously to
384 [U-^{15}N]-*hs* CIB2 (Figure 7C, Figure 7-figure supplement 7B). We observed similar results when
385 comparing spectra for [U-^{15}N]-*hs* CIB3 alone, co-refolded with *hs* TMC1-IL1, and upon addition
386 of *hs* TMC1-NT (Figure 7-figure supplement 7C-D). A control experiment with the co-refolded
387 mix of *hs* CIB3 + *hs* TMC1-IL1 and [U-^{15}N]-*hs* CIB2 (Figure 7-figure supplement 7E) revealed
388 no change in chemical shifts indicating that direct heteromeric interactions between CIB2 and
389 CIB3 are unlikely. Thus, taken together, the NMR data strongly support a model in which human
390 CIB2/3 proteins are clamped between TMC1-IL1 and TMC1-NT as suggested by AF2 and
391 consistent with prior biochemical data revealing interactions with either TMC1-NT or TMC1-IL1
392 (Giese et al., 2017; Liang et al., 2021).
393
394 **Simulations reveal CIB proteins stabilize TMC1 and TMC2**
395 Our dimeric AF2 models of TMC1/2 alone and in complex with CIB2/3 are consistent with
396 previous experimental data that validated the location of the putative pore in similar
397 TMEM16/OSCA-based homology models of TMC1 (Pan et al., 2018). Our models are also
398 consistent with our NMR data supporting the clamp model for the TMC + CIB complex (Figure
399 7C). To improve the AF2 predictions and to gain mechanistic insights into TMC and CIB function
400 we turned to all-atom equilibrium molecular dynamics (MD) simulations (Karplus and Petsko,
401 1990). We built ten different models that included dimeric TMC1 or TMC2 alone, in complex with
402 CIB2 or CIB3 with and without bound Ca^{2+}. These models were embedded in either pure POPC
403 or stereocilia-like mixed composition bilayers and solvated (150 mM KCl) to generate a total of
404 twenty systems that were equilibrated for 100 ns each (Figure 8A, Figure 8-table supplement 1).

405 Equilibrium simulations of TMC1 and TMC2 alone revealed stable conformations for the
406 transmembrane domains of these proteins, but a highly mobile NT domain (Figure 8B, Figure 8-
407 figure supplement 1). In simulations where CIB2 or CIB3 were present, with or without bound
408 Ca^{2+}, we observed more stable conformations of N-termini along with stable salt bridges (Figure
409 8C). Buried surface area (BSA) for the TMC + CIB complexes (Figure 8-figure supplement
410 2A,C,E, Figure 8-table supplement 2) revealed a possible trend in which TMC1 and TMC2 have
411 more contacts with CIB3 than with CIB2. While additional sampling and longer simulations might
412 be needed for a robust prediction, these results suggest variable affinities for TMC + CIB protein
413 complexes that might be modulated by Ca^{2+} (Figure 8-figure supplement 2F).
414 Additional analysis of the putative pore in our simulations of TMC1 and TMC2 revealed
415 hydration as observed in previous simulations of TMEM16/OSCA-based TMC1 models, as well
416 as movement of lipids that lined up the predicted permeation pathway for cations suggesting a
417 membrane-based gating mechanism (Pan et al., 2018; Sukharev and Corey, 2004; Walujkar et al.,
418 2021). Longer, Anton 2, 960-ns long equilibrium trajectories of TMC1 with CIB2 and bound Ca^{2+}
419 in a mixed bilayer and TMC1 with CIB2 and (un)bound Ca^{2+} in a POPC bilayer revealed how
420 parts of the amphipathic α0 helices spontaneously partitioned at the membrane interface with their
421 hydrophobic sides pointing toward the lipid bilayer core (Figure 8D). The N-terminal cytoplasmic
422 domain of LHFPL5 has been shown to interact with this TMC1 amphipathic helix, which might
423 be essential for channel function in mice (Qiu et al., 2023). The BSA for the dimeric TMC1 +
424 CIB2 complex in these longer simulations (Figure 8-figure supplement 2E) decreased as contacts
425 between TMC1-α0 and CIB2 were lost for one of the monomers in the mixed bilayer system. In
426 the monomer in which contacts were maintained, a single cholesterol was situated in the middle
427 of the putative pore. Similarly, TMC1-α0 and CIB2 contacts were lost for both monomers in the

428 POPC bilayer systems. Regardless, in all Anton 2 equilibrium trajectories contacts between CIB2
429 and the TMC1-IL1 and -NT remained, thus confirming the stability of the complex over a
430 microsecond timescale.
431
432 **TMC1 and TMC2 complexes with CIB2 and CIB3 are predicted to be cation channels**
433 To further explore the properties of our models of TMC/CIB complexes we took
434 equilibrated TMC1 systems and applied a -0.5 V transmembrane voltage while monitoring ion
435 permeation through the putative pore during 100-ns long trajectories (Figure 8-figure supplements
436 3-4, Figure 8-table supplement 2, Figure 8-video 2). In systems with pure POPC bilayers we
437 observed permeation of K^+ in either one or both pores of the TMC1 dimer, with or without CIB2
438 or CIB3 and with or without bound Ca^{2+}, despite the presence of Cl^- (150 mM KCl). Similar results
439 were obtained for four TMC1 systems simulated at -0.25 V. Variability of the conductance state
440 was attributed to partial blockage by lipids and poor sampling, but in all cases in which a clear
441 conductive state was monitored we observed almost exclusive passage of K^+ with conductance
442 values that reached up to ~138 pS for a single pore. While simulations tend to overestimate bulk
443 KCl conductivity and in some cases predictions need to be scaled down (by a factor of ~0.6)
444 (Walujkar et al., 2021), the conductance values monitored here are consistent with previous
445 simulations and with the expected conductance of the inner-ear transduction channel (Beurg et al.,
446 2021; Walujkar et al., 2021). In contrast, we observed smaller conductance values for TMC1
447 systems with mixed lipid bilayers (at most ~22 pS for a single pore), regardless of the presence of
448 CIB2 or CIB3, with or without bound Ca^{2+} (Figure 8-figure supplement 4B). Additional Anton 2
449 simulations for one of these TMC1 + CIB2 + Ca^{2+} systems with a mixed membrane, equilibrated
450 for 240 ns and then subjected to -0.43 V for 480 ns, revealed a low conductance value of ~6.2 pS.

451 The reduced conductance values observed for mixed-membrane systems were attributed in part to
452 pore blockage by cholesterol and lipids in the initial setup. Interestingly, Anton 2 simulations of
453 TMC1, TMC1 + CIB2, and TMC1 + CIB2 + Ca^{2+} in pure POPC membranes subjected to -0.5 V,
454 -0.25 V, and -0.125 V for 480 ns, 480 ns, and 960 ns, respectively, revealed a trend in which TMC1
455 exhibits higher conductance with CIB2 bound (Figure 8E, Figure 8-table supplement 2). This may
456 begin to explain why CIB2 is essential for normal TMC1 function.

457 Simulations of TMC2 with an applied transmembrane voltage of -0.5 V revealed a more
458 closed state when compared to our TMC1 model, regardless of membrane composition and
459 presence or absence of CIB2, CIB3 and bound Ca^{2+} (Figure 8-figure supplement 4). Conduction
460 of K^+ was observed in most cases, but the maximum conductance did not reach above ~42 pS,
461 suggesting that the conformation simulated is less open than the ones explored in simulations of
462 TMC1. We also speculate that this is due to TMC2 having an intrinsic lower single-channel
463 conductance than TMC1, as has been suggested by some experiments (Kim et al., 2013), but not
464 others (Pan et al., 2013). It is also possible that our TMC2 model is not in a fully open
465 conformation, which can only be reached upon mechanical stimulation. Regardless, our
466 simulations unequivocally indicate that TMC1 and TMC2 are cation channels and that these
467 proteins can form stable complexes with CIB2 and CIB3.

468

469 **Discussion**

470 Previous work on CIB proteins had primarily focused on mammalian auditory hair cells,
471 leaving open the question of whether they play a functional role in vestibular function and across
472 vertebrate species. Recently, Wang et al. have suggested that CIB2 and CIB3 are important for
473 stereocilia maintenance and MET in mouse vestibular hair cells (Wang et al., 2023). This work

474 demonstrated that similar to *Tmc1* and *Tmc2*, *Cib2* is highly expressed in the striolar region while
475 *Cib3* is expressed in the extrastriolar regions, and mice lacking both *Cib2* and *Cib3* had no MET
476 and deficits in vestibular hair cell bundle structure (Wang et al., 2023). Taking a step forward, here
477 we establish that CIB2 and CIB3 are highly conserved regulators of MET in both mouse vestibular
478 hair cells and zebrafish hair cells. We demonstrate that vestibular hair cells in mice and zebrafish
479 lacking CIB2 and CIB3 are not degenerated but have no detectable MET, assessed via FM 1-43
480 dye uptake, at time points when MET function is well developed in wild-type hair cells. Similar
481 structural-function phenotype has been reported in auditory hair cells in *Tmc1/Tmc2* double mutant
482 mice (Kawashima et al., 2015). Besides the known *in vitro* interactions (Giese et al., 2017; Liang
483 et al., 2021), our study provides strong genetic evidence for the direct functional relationship
484 between CIB and TMC proteins in regulating MET both in auditory and vestibular hair cells.

485 Previous studies have shown that the loss of CIB2 leads to profound hearing loss from birth
486 in both human and mice (Giese et al., 2017; Liang et al., 2021; Seco et al., 2016). This suggests
487 that the endogenous levels of CIB3 present in auditory hair cells are not sufficient to compensate
488 for CIB2 in hearing. Prior work has also shown that over-expression of CIB3 in mouse auditory
489 outer hair cells can only partially compensate for the loss of CIB2 in MET (Liang et al., 2021).
490 However, whether overexpression of CIB3 can rescue impaired hearing thresholds in *Cib2* mutant
491 mice is not known. While CIB2 is also present in vestibular hair cells, compared to auditory hair
492 cells, the expression of CIB3 is several folds higher in vestibular end organs. Indeed, our current
493 data demonstrate that, unlike auditory hair cells, endogenous levels of CIB3 can fully compensate
494 for loss of CIB2 in vestibular hair cells in mice. Together our work on the vestibular system in
495 mice highlights that both CIB2 and CIB3 can play overlapping roles in MET function.

496 Interestingly, our corresponding work in zebrafish indicates that Cib3 can also compensate
497 for Cib2, but only in specific subsets of hair cells. Recent genetic, morphology and scRNAseq data
498 have revealed that within the zebrafish inner ear, each sensory epithelia (utricle, saccule, cristae)
499 has distinct groups of hair cells (Shi et al., 2023; Smith et al., 2020). In crista of the zebrafish inner
500 ear, which respond to angular acceleration, there are two main groups of hair cells that can be
501 delineated by distinct morphological and genetic features. Morphologically these two group are
502 defined as either short or tall hair cells (Figure 6A,E). Genetic studies have revealed that these two
503 types of hair cells rely on different Tmc combinations for MET–short cells rely on Tmc2a while
504 tall cells rely on Tmc2b and Tmc1 (Smith et al., 2020). More recent mRNA *in situ* studies have
505 validated this *Tmc* requirement and shown that *tmc2a, tmc2b, tmc1* are expressed in just tall cells,
506 while *tmc2a* is only expressed in short cells (Smith et al., 2023). Interestingly, this work also
507 demonstrated that *cib2* is expressed broadly in tall and short hair cells, while *cib3* showed more
508 restricted expression in tall hair cells. Our work on MET in the zebrafish cristae indicates that Cib2
509 is required in both short and tall cells, while Cib3 is required in just tall cells. This expression data
510 set is supported by absence of FM 4-64 labeling from short hair cells when Cib2 is lost (Figure
511 6H). In contrast, loss of Cib3 alone does not impact FM 4-64 labeling in the zebrafish crista,
512 indicating that Cib2 can compensate for loss of Cib3 in both short and tall cells (Figure 6G).
513 Currently it is not clear what role different types of hair cells play in zebrafish inner ear epithelia.
514 Our present findings show that zebrafish *cib2* mutants have a severely diminished acoustic startle
515 response, a behavior mediated primarily by the saccule (Figure 5A). These behavioral results
516 suggest that Cib2 plays an important role in hair cells that detect acoustic stimuli.

517 In addition to the inner ear, we likewise found that both Cib2 and Cib3 play an important
518 role in the zebrafish lateral line. Similar to the zebrafish inner ear and mouse vestibular system,

519 we show that in lateral-line hair cells, Cib2 can compensate for MET in all hair cells when Cib3 is
520 lost (Figure 5B,C,F,K, Figure 5-figure supplement 2A-C). However, like in the zebrafish inner ear,
521 when Cib2 is lost, MET is lost from a specific population of lateral-line hair cells. In the lateral
522 line, each neuromast has two cell populations that detect flow in opposing directions (López-Schier
523 and Hudspeth, 2006; Pujol-Martí and López-Schier, 2013). Work in the posterior lateral line has
524 demonstrated that cells that detect anterior flow rely on Tmc2a/2b for MET, while cells that detect
525 posterior flow rely on just Tmc2b (Chou et al., 2017). In our work we find that cells that detect
526 anterior flow primarily rely on Cib2 for MET (Figure 6C-D). Further, this work indicates that Cib3
527 cannot compensate for loss of Cib2 in these cells. Interestingly, our functional assessment in the
528 zebrafish lateral line and crista suggests that Cib2 is specifically required for mechanosensitive
529 function in populations of hair cells that express Tmc2a. Whether Cib3 is unable to pair with
530 Tmc2a or is simply not expressed along with Tmc2a remains an unanswered question. The
531 significance of this pairing is also unclear. Recent work has shown that the addition of Tmc2a to
532 lateral-line cells that detect anterior flow significantly augments the mechanosensitive responses
533 of these cells (Kindig et al., 2023). Whether Cib2 is required along with Tmc2a for these
534 augmented responses remains unclear.

535 Our *in vivo* studies of mouse TMC + CIB and zebrafish Tmc + Cib complexes suggest a
536 conserved functional relationship between these two protein families across vertebrates. Structural
537 predictions using AF2 show conserved folds for human and zebrafish proteins, as well as
538 conserved architecture for their protein complexes. Predictions are consistent with previous
539 experimentally validated models for the TMC1 pore (Ballesteros et al., 2018; Pan et al., 2018),
540 with the structure of human CIB3 coupled to mouse TMC1-IL1 (Liang et al., 2021), and with our
541 NMR data validating the interaction between human TMC1 and CIB2/3 proteins. Remarkably, the

542 AF2 models are also consistent with the architecture of the nematode TMC-1 and CALM-1
543 complex (Jeong et al., 2022), despite low sequence identity (36% between human TMC1 and worm
544 TMC-1 and 51% between human CIB2 and worm CALM-1). This suggests that the TMC + CIB
545 functional relationship may extend beyond vertebrates.

546 Taken together, the modeling predictions, NMR experiments, and simulations presented
547 here provide a structural framework to interpret and understand seemingly contradictory results.
548 In a previous study (Giese et al., 2017), we showed that the N-termini of TMC1 and TMC2 interact
549 with CIB2, and subsequent work (Liang et al., 2021) presented biochemical data validating the
550 interaction between the TMC1-NT with CIB2. However, X-ray crystallography data demonstrated
551 that the main interaction between TMC1 and CIB3 involved IL1, leaving the role played by CIB2-
552 TMC-NT interactions unaddressed (Liang et al., 2021). Here we show using NMR that both
553 TMC1-NT and TMC1-IL1 bind to CIB2 and CIB3 non-competitively. These interactions are
554 consistent with AF2 models for TMC + CIB complexes where CIB proteins are clamped between
555 TMC1-NT and IL1. Simulations of these models indicate that there is some potential preferential
556 binding of TMC1 and TMC2 to CIB3 over CIB2 (predicted from BSA) and that TMC + CIB
557 interactions are stable and last for microseconds, with biochemical and NMR experiments showing
558 that these interactions are stable at even longer timescales.

559 Interestingly, the behavior of CIB2 and CIB3 in solution (SEC experiments using 3 mM
560 $CaCl_2$) is different in the absence of TMC1-IL1. While CIB2 appears as a single peak, CIB3 shows
561 two clear peaks indicating the presence of monomeric and dimeric states, consistent with the
562 crystal structure of an apparent CIB3 dimer (Liang et al., 2021). In the presence of TMC1-IL1, the
563 CIB3 dimeric peak is absent, and the potentially monomeric peak is slightly shifted accounting for

564 the added TMC1-IL1, as observed for CIB2. This result suggests that CIB2, both in the presence
565 and in the absence of TMC1-IL1, is monomeric in solution (Figure 7-figure supplement 6). This
566 proposal is consistent with prior conclusions that CIB2 is a monomer (Dal Cortivo et al., 2019),
567 but is in disagreement with other reports indicating that CIB2 is a dimer in solution (Vallone et al.,
568 2018) and our own prior pull-down assays indicating that CIB2 co-immunoprecipitated with
569 differentially tagged CIB2 or CIB3 (Giese et al., 2017; Riazuddin et al., 2012). Moreover, our
570 NMR data (obtained using 3 mM $CaCl_2$) indicates that TMC1-IL1 + CIB2 is unlikely to directly
571 interact with CIB3. The simplest explanation for these seemingly contradictory results comes from
572 the TMC1 and TMC2 dimeric states (Pan et al., 2018) and our modeling indicating that each TMC
573 monomer interacts with one CIB protein (Figure 7-figure supplement 1). Pull-down assays might
574 simply be reflecting the oligomeric state of TMC proteins. In such scenario, and considering that
575 TMC proteins have been suggested to form hetero-oligomers (Pan et al., 2018), there are up to ten
576 different combinations of TMC1/2 and CIB2/3 proteins (Figure 8-figure supplement 5) that might
577 have distinct properties. Such variety of complexes with potentially different conductance values
578 might explain tonotopic changes of conductance along the cochlea, although other explanations
579 exist, including a variable number of TMC proteins around the tip link (Beurg et al., 2018) and the
580 direct influence of membrane composition on conductance (Effertz et al., 2017; Walujkar et al.,
581 2021).

582 How TMC + CIB interactions depend on Ca^{2+} concentration may have important functional
583 implications for adaptation and hair cell mechanotransduction. Structures of CIB3 and worm
584 CALM-1, a CIB2 homologue, both bind divalent ions via EF-hand motifs proximal to their C-
585 termini (Jeong et al., 2022; Liang et al., 2021). Reports on CIB2 affinities for Ca^{2+} are inconsistent,
586 with K_D values that range from 14 μM to 0.5 mM (Blazejczyk et al., 2009; Vallone et al., 2018).

587 Although qualitative pull-down assays done in the presence or the absence of 5 mM $CaCl_2$ suggest
588 that the TMC1 and CIB2 interactions are Ca^{2+}-independent (Liang et al., 2021), strength and
589 details of the CIB-TMC-IL1 and CIB-TMC-NT contacts might be Ca^{2+}-dependent, especially
590 considering that Ca^{2+} induces changes that lead to exposure of hydrophobic residues involved in
591 binding (Blazejczyk et al., 2009).

592 Our simulations in the presence of a biasing potential unequivocally demonstrate that both
593 TMC1 and TMC2, in the presence or the absence of CIB proteins, with or without bound Ca^{2+},
594 and in two types of membranes, are cation channels with predicted single-channel conductance
595 values that can reach values that are consistent with those of the transduction channel. Our models
596 emphasize again the role played by the membrane in lining the pore of TMC proteins (Pan et al.,
597 2018; Walujkar et al., 2021), and also indicate that CIB proteins are ideally positioned to connect
598 various parts of cytosolic inter-helix linkers with the helices that form the pore, specially α3 and
599 α4, recently implicated in gating (Akyuz et al., 2022; Walujkar et al., 2021). Last, our modeling
600 also positions the myristoylated N-terminus of CIB2 and CIB3 close enough to the membrane
601 bilayer, which might be yet another way to sense membrane stretch and influence gating. Further
602 studies should help provide a comprehensive view into CIB function in channel assembly,
603 activation, and potentially hair-cell adaption.

604 Overall, the biochemically supported atomic-resolution structural models and simulations
605 presented here along with our results obtained using animal models strongly suggest that TMC1/2
606 proteins must function with CIB2/3 in normal hair-cell MET across sensory organs, hair-cell types,
607 and species. This is supported by structural data indicating multiple contact points between TMC
608 and CIB proteins, simulation data predicting that CIB proteins stabilize TMC cytosolic domains

609 and may enhance cation conduction, and *in vitro* and *in vivo* functional data indicating that both

610 TMC1/2 and CIB2/3 proteins are needed for hair-cell MET.

611 **Materials and methods**

612 **Key resources table**

REAGENT or RESOURCE	SOURCE	IDENTIFIER
Antibodies		
Goat anti-Mouse IgG (H+L) Highly Cross-Adsorbed Secondary Antibody, Alexa Fluor 568	Thermo Fisher Scientific	Cat#A-11031; RRID: AB_144696
Goat anti-Mouse IgG (H+L) Secondary Antibody, Alexa Fluor 488	Thermo Fisher Scientific	A32723
Goat anti-Rabbit IgG (H+L) Highly Cross-Adsorbed Secondary Antibody, Alexa Fluor 488	Thermo Fisher Scientific	Cat#A-11034; RRID: AB_2576217
Goat anti-rabbit IgG (H+L) Secondary Antibody, Alexa Fluor 568	Thermo Fisher Scientific	A-11011
Mouse monoclonal anti-FLAG M2	Sigma-Aldrich	Cat#F3165; RRID: AB_259529
Mouse monoclonal anti-FLAG M2-HRP	Thermo Fisher Scientific	Cat#A8592; RRID: AB_439702
Mouse monoclonal anti-V5	Thermo Fisher Scientific	Cat# R960-25; RRID: AB_2556564
Mouse monoclonal anti-V5-HRP	Thermo Fisher Scientific	Cat#R961-25; RRID: AB_2556565
Mouse monoclonal GAPDH	Santa Cruz	sc-32233
Rabbit polyclonal anti-CIB3	Sigma	SAB2103524
Rabbit polyclonal anti-GFP	Invitrogen	A-11122
Rabbit polyclonal anti-GFP-HRP	Thermo Fisher Scientific	Cat#A10260; RRID: AB_2534022
Rabbit polyclonal anti-Myosin VIIa	Proteus Biosciences	#25-6790
Rabbit polyclonal anti-V5	Abcam	Cat#ab9116; RRID: AB_307024
Chemicals		
FM™ 1-43FX	Thermo Fisher Scientific	F35355
FM™ 1-43	Thermo Fisher Scientific	T3163
FM™ 4-64	Thermo Fisher Scientific	T13320
Alexa Fluor™ 488 Phalloidin	Thermo Fisher Scientific	A12379

Alexa Fluor™ 633 Phalloidin	Thermo Fisher Scientific	A22284
16% Paraformaldehyde	Electron Microscopy Sciences	50-980-487
Triton X-100	Polysciences	04605-250
DAPI (4',6-Diamidino-2-Phenylindole, Dihydrochloride)	Invitrogen	D1306
Protease inhibitor mixture	Roche	11697498001
Protein A–Sepharose CL-4	Thermo Fisher Scientific	101042
Polyethylenimine	Polysciences	23966
Critical Commercial Assays		
4–20% Tris-Glycine gel	Novex	XV04205PK20
SMARTScribe Reverse Transcriptase kit	Clontech	639537
SYBRgreen technology	Qiagen	330503
Amersham™ ECL™ Prime Western Blotting Detection Reagent	GE Healthcare	RPN2236
QIAshredder	Qiagen	Cat#79656
Trans-Blot® Turbo™ Transfer System	Bio-Rad	Cat#1704156
Trans-Blot® Turbo™ Midi PVDF Transfer Packs	Bio-Rad	Cat#1704157
4–20% Mini-PROTEAN® TGX Stain-Free™ Protein Gels	Bio-Rad	Cat#4568094
4–20% Criterion™ TGX Stain-Free™ Protein Gel	Bio-Rad	Cat#5678094
GFP-Trap Magnetic Agarose	Chromotek	Cat#gtma-20
Anti-v5 agarose affinity gel	Sigma-Aldrich	Cat#A7345
Anti-FLAG® M2 Magnetic Beads	Sigma-Aldrich	Cat#M8823
Nunc™ Lab-Tek™ chambered coverglass	Thermo Fisher Scientific	Cat#155411PK
Lipofectamine™ 3000 Transfection Reagent	Thermo Fisher Scientific	Cat#L3000015
Experimental Models: Organisms/Strains		
Cib2^{tm1a}	EUCOMM	
Cib3^{KO}	This study	N/A
cib2^{idc21} zebrafish	This study	N/A
cib3^{idc22} zebrafish	This study	N/A
Tg(myo6b:GCaMP6s-CAAX)^{idc1} zebrafish	(Sheets et al., 2017)	ZDB-ALT-170113-3

613

614 **<u>Mouse strains and husbandry</u>**

615 *Cib2*^{KO} mice: *Cib2* $^{tm1a(EUCOMM)Wtsi}$ mice were obtained from the EUCOMM repository and
616 maintained on C57BL/6 N background. A gene trap cassette containing lacZ and neomycin
617 resistance genes flanked by FRT sites was inserted downstream of exon 3, with exon 4 flanked by
618 loxP sites.

619 *Cib3*^{KO} *mice: Cib3* knockout mice were generated using CRISPR/Cas9 technology. An
620 indel in exon 4 of *Cib3* was introduced leading to a nonsense mutation and a premature stop at the
621 protein level (p.Asp54*). Primers used to genotype Cib3 mutant mice were F:
622 GTAGGGGCATGGATAACATCTG and R: GTTGAATGCTTGTCTCCCCAGG. *Cib3*^{KO} mice
623 were backcrossed using C57Bl6/JN *Cib2*^{KO} mice for several generations. *Cib3* allele was validated
624 at the genomic, RNA messenger, and protein level.

625 Animals were group-housed with their littermates on a 12:12 h light: dark cycle at 20°C
626 with ad libitum access to food and water. All animal procedures were approved by the Institutional
627 Animal Care and Use Committees (IACUCs) at University of Maryland (protocol #0420002) and
628 at Harvard Medical School (protocol #00001240).

629

630 **Western blot and qPCR in mice**

631 Mouse heart tissues were homogenized in CHAPS buffer containing 1X protease inhibitors, 1 mM
632 Na orthovanadate, 10 mM Na glycerophosphate, and 10 mM NaF. Equivalent protein
633 concentrations were fractionated on a 4–20% Bis–Tris gel (Invitrogen) and transferred to
634 polyvinylidene fluoride (PVDF) membrane (Millipore). Membranes were blocked and then probed
635 with the rabbit anti-CIB2 (1:500), CIB3 (1:500), and GAPDH (1:500) overnight at 4ºC, followed
636 by three washes of 30 min each in 1X TBST. After washing, blots were incubated with horseradish
637 peroxidase-conjugated anti-rabbit antibody (1:1000, Sigma NA934V, Lot # 17640116) for 2 h at

638 room temperature, followed by detection using the ECL Prime Western Blotting System (Thermo
639 Fisher Scientific 32,106).
640 RNAs from brain were extracted from *Cib2;Cib3* mutant and control mice using the
641 Ribopure kit (Ambion). SMARTScribe Reverse Transcriptase kit (Clontech) was used to generate
642 cDNAs, and SYBRgreen technology (Qiagen) was used to perform the qPCR. The following
643 primers were used to amplify *Cib2* and *Cib3*: Cib2_exon4_F: CTCTGTGCTCTGCGAATCAG,
644 Cib2_exon5_R: GGCCAGCGTCATCTCTAAGT, Cib3_exon3_F:
645 TGGTGCCTCTTGACTACACG, Cib3_exon5_R: CAGCACCTTCTCACAGACCA. *hprt*
646 amplification was used to normalize the samples: hprt_exon8_F:
647 TGTTGTTGGATATGCCCTTG, hprt_exon9_R: GGCTTTGTATTTGGCTTTTCC.
648
649 **Quantification of VOR and OKR in mice**
650 Surgical techniques and experimental setup have been previously described (Beraneck and Cullen,
651 2007). Eye movement data were collected using an infrared video system (ETL-200, ISCAN
652 system). The rotational velocity of the turntable (head velocity) was measured using a MEMS
653 sensor (MPU-9250, SparkFun Electronics). Eye movements during OKR were evoked by
654 sinusoidal rotations of a visual surround (vertical black and white stripes, visual angle width of 5°)
655 placed around the turntable at frequencies 0.2, 0.4, 0.8, 1, and 2 Hz with peak velocities of ±16◦/s.
656 To record VOR responses, the turntable was rotated at sinusoidal frequencies 0.2, 0.4, 0.8, 1, and
657 2 Hz with peak velocities of ±16◦/s in both light and dark. In the light condition, the visual surround
658 remained stationary, whereas in the dark condition, both the visual surround and turntable rotated
659 in phase. Head and eye movement signals were low-passed filtered at 125 Hz and sampled at 1
660 kHz. Eye position data were differentiated to obtain velocity traces. Cycles of data with quick

661 phases were excluded from the analysis. Least-square optimization determined the VOR and OKN
662 gains and phases (Beraneck et al., 2008) plotted as mean ± standard deviation (SD) against all
663 frequencies for all mice. *Cib2*$^{+/+}$; *Cib3*$^{KO/KO}$ (*n* = 4), *Cib2*$^{KO/+}$; *Cib3*$^{KO/KO}$ (*n* = 5), and *Cib2*$^{KO/KO}$;
664 *Cib3*$^{KO/KO}$ (*n* = 4) mice were tested for all frequencies. Two-way ANOVAs and Bonferroni post
665 hoc tests were used to test statistical significance.
666
667 **Mouse rotarod test**
668 *Cib2*$^{+/+}$;*Cib3*$^{KO/KO}$ (n = 6), *Cib2*$^{KO/+}$;*Cib3*$^{KO/KO}$ (n = 6), and *Cib2*$^{KO/KO}$;*Cib3*$^{KO/KO}$ (n = 6) mice were
669 used. Motorized rotating rod (Rotarod, IITC Life Science) was programmed to accelerate from 4
670 rpm to 40 rpm with a ramp of 300 s for each test trial. The time taken for a mouse to fall off the
671 rotarod was recorded. Three trials were performed each day for 5 consecutive days. First day (day
672 0) was considered the training day.
673
674 **Quantification of head motion in mice**
675 Head motion was recorded in mice via a miniature motion sensor (MPU-9250, TDK Corporation)
676 attached to the top of the skull. The motion sensor recorded 3-axis linear acceleration (i.e., fore-
677 aft, lateral, and vertical) and 3-axis angular velocity (roll, pitch, and yaw) at 100 Hz sampling rate.
678 The power spectra of the motion signals in all six dimensions were computed using Welch's
679 averaged periodogram with nfft = 512 and a Bartlett window (pwelch function, MATLAB,
680 MathWorks).
681
682 **Circling behavior in mice**

683 Mice were placed in a cylindrical-shape container (27 cm in diameter, 30 cm in height) and their
684 behavior were recorded using a cell-phone camera. The number of rotations made during 120-
685 second recording were counted offline by watching the recorded videos. A rotation is defined as a
686 completed 360-degree rotation of the mouse's heading.
687
688 **Immunostaining in mice**
689 The cochlear and vestibular sensory epithelia were isolated, fine dissected and permeabilized in
690 0.25% Triton X-100 for 1 h and blocked with 10% normal goat serum in PBS for 1 h. The tissue
691 samples were probed with primary antibody overnight and after three washes were incubated with
692 the secondary antibody for 45 min at room temperature. Rhodamine phalloidin or Alexa fluor
693 phalloidin 488 were used at a 1:250 dilution for F-actin labeling. Nuclei were stained with DAPI
694 (Molecular Probes). Images were acquired using either LSM 700 laser scanning confocal
695 microscope (Zeiss, Germany) with a 63× 1.4 NA or 100× 1.4 NA oil immersion objectives or
696 Leica SP8 laser scanning confocal microscope with a 100× 1.44 NA objective lens. Stacks of
697 confocal images were acquired with a Z step of 0.05-0.5 µm and processed using ImageJ software
698 (National Institutes of Health). Experiments were repeated at least 3 times, using at least three
699 different animals.
700
701 **FM 1-43 dye uptake experiments in mice**
702 In the Ahmed lab, cochlear explants from *Cib2* and *Cib3* mutant mice were dissected at postnatal
703 day 5 (P5) and cultured in a glass-bottom petri dish (MatTek, Ashland, MA). They were
704 maintained in Dulbecco's modified Eagle medium (DMEM) supplemented with 10% FBS (Life
705 Technologies) for 2 days at 37 °C and 5% CO_2. Explants were incubated for 10 s with 3 µM FM

706 1-43, washed three times with Hank's balanced salt solution, and imaged live using a Zeiss LSM
707 700 scanning confocal microscope.
708 In the Holt Lab, P60 mice were injected intraperitoneally with 5 mg/g mouse weight of FM
709 1-43FX fixable form as previously described (Meyers et al., 2003). Tissue was collected after ~24
710 h and fixed for 1 h at 25 °C in 4%PFA/1X PBS protected from light. Tissue was then transferred
711 into 120 mM EDTA pH 7.4 for 48-72 h protected from light. Then tissue was transferred to
712 1XPBS, dissected, incubated in 1:1000 dilution of Phalloidin (Invitrogen), washed three times in
713 1XPBS and mounted under glass coverslips for microscopy. Imaging was completed using a 20×
714 objective on a Zeiss 800 confocal microscope with laser intensity, detector gain, and post
715 processing set equally for each sample.
716
717 **ABR measurements in mice**
718 Hearing thresholds of *Cib2* and *Cib3* mutant mice ($n = 5–10$ each genotype) were evaluated by
719 recording ABRs. All ABR recordings, including broadband clicks and tone-burst stimuli at three
720 frequencies (8, 16, and 32 kHz), were performed using an auditory-evoked potential RZ6-based
721 auditory workstation (Tucker-Davis Technologies) with high frequency transducer RA4PA
722 Medusa PreAmps. Maximum sound intensity tested was 100 dB SPL. TDT system III hardware
723 and BioSigRZ software (Tucker Davis Technology) were used for stimulus presentation and
724 response averaging.
725
726 **Zebrafish strains and husbandry**

727 Zebrafish (*Danio* rerio) were grown at 28°C using standard methods. Zebrafish were maintained
728 in a Tubingen or TAB background. Larvae were raised in E3 embryo medium (5 mM NaCl,
729 0.17 mM KCl, 0.33 mM $CaCl_2$, and 0.33 mM $MgSO_4$, buffered in HEPES, pH 7.2). Zebrafish work
730 at the National Institute of Health (NIH) was approved by the Animal Use Committee at the NIH
731 under animal study protocol #1362-13. All experiments were performed on larvae at 5-6 days post
732 fertilization (dpf). At this age sex determination is not possible. Neuromasts (L1-L5) in the primary
733 posterior lateral line were used for our analyses. For Ca^{2+} imaging the following transgenic line
734 was used: *Tg(myo6b:memGCaMP6s)*^{idc1} (Jiang et al., 2017).

735 *Cib2*^{idc21} and *cib3*^{idc22} mutants were generated in-house using CRISPR-Cas9 technology as
736 previously described (Varshney et al., 2016). Exon 3 and exon 6 were targeted for *cib2* and *cib3*
737 respectively. Guides for *cib2* and *cib3* are as follows: 5'-GGAGGAGCTTACACCAG(AGG)-3'
738 and 5'-GGAAATCCTCCAGAGAAAGG(CGG)-3'. Founder fish were identified using fragment
739 analysis of fluorescent PCR products (Varshney et al., 2016). Founder fish containing a 10 bp
740 insertion in *cib2* 5'-GCTTACACCA(<u>CCTTTGGTAG</u>)GAGGAGGTTA-3' resulting in a stop
741 codon in the third EF-hand domain, at amino acid 148, was selected for analysis (Figure 5-figure
742 supplement 1). In addition, a founder fish containing a 4 bp deletion in *cib3* 5'-
743 TGGCCGCCT(TTCT)CTGGAGG-3' resulting in a stop codon in the third EF-hand domain, at
744 amino acid 159, was selected for analysis (Figure 5-figure supplement 1). After behavior or
745 imaging analyses, genotypes were confirmed using standard PCR and sequencing. The following
746 primers were used for genotyping: *cib2*_FWD 5'- ACTGAAGCAACTCCTTTTGTGG-3' and
747 *cib2*_REV 5'-GAACCATGCATTTTTACAGC-3' and *cib3*_FWD 5'-
748 ATAGTCTCTCCATCTATAGACT-3' and *cib3*_REV 5'-TTTTAGGGTGAAATAAAACAGA-
749 3'. Crosses of *cib2*$^{+/-}$;*cib3*$^{-/-}$ X *cib2*$^{+/-}$;*cib3*$^{+/-}$ or *cib2*$^{-/-}$;*cib3*$^{+/-}$ X *cib2*$^{+/-}$;*cib3*$^{+/-}$ adults were used

750 to propagate larvae for our analyses. All controls or siblings are double heterozygous animals.
751 Larvae were chosen at random, except for *cib2;cib3* homozygous mutants which, similar to other
752 zebrafish mutants with hearing and balance defects, had no swim bladder and no acoustic startle
753 response.
754
755 **Labeling zebrafish hair cells with FM 1-43, FM 4-64, and FM 1-43FX**
756 To label lateral-line hair cells with FM 1-43, larvae were immersed in 1 μM FM 1-43
757 (ThermoFisher, T3163) in E3 for 30 s, and then washed 3 times in E3. After washing, larvae were
758 mounted in 1% low melt agarose containing an anesthetic, 0.02% tricaine methanesulfonate
759 (Syndel, ANADA 200-226). FM 1-43 labeled hair cells were then imaged on an A1 Nikon upright
760 laser-scanning confocal microscope with a 60× 1.0 NA water objective. FIJI was used to process
761 image Z-stacks. To estimate the number of hair cells per neuromast, laser scanning DIC images
762 were used to count the number of hair bundles per neuromast. To quantify FM 1-43 label, a 5 μm
763 circular region of interest (ROI) was placed on the soma of each hair cell with a hair bundle in the
764 DIC image. These ROIs were used to quantify the mean FM 1-43 intensity per hair cell. These
765 intensity values were averaged to calculate the average FM 1-43 intensity per neuromast.
766 FM 4-64 (ThermoFisher, T13320) was used to label hair cells in the crista within the
767 zebrafish inner ear. For this labeling, *Tg(myo6b:memGCaMP6s)*^{idc1} larvae were mounted on their
768 side on Sylgard chamber in E3 embryo media containing 0.02% MESAB. Approximately 2-3 nL
769 of 10 μM FM 4-64 in 0.1 M KCl were injected into the otic capsule as previously described (Smith
770 et al., 2020). FM 4-64 labeled hair cells of the medial crista were then imaged on an A1 Nikon
771 upright laser-scanning confocal microscope with a 25× 1.10 NA or 60× 1.0 NA water objective.

772 FIJI was used to process image Z-stacks. To assess tall versus short hair cells in each crista
773 *memGCaMP6s* label was used.
774 To correlate hair bundle orientation in lateral line hair cells with intact
775 mechanotransduction, larvae were immersed in 3 μM FM 1-43FX (ThermoFisher, F25255) in E3
776 for 30 s, and then washed 3 times in E3. After washing, larvae were fixed with 4%
777 paraformaldehyde in PBS at 4°C overnight. After fixation, larvae were washed 4 × 5 min in 0.1%
778 Tween in PBS (PBST). Larvae were then placed in blocking solution (2% goat serum, 1% bovine
779 serum albumin, 2% fish skin gelatin in PBS + 0.3% triton) for 2 h at room temperature. After block
780 Alexa Fluor 633 Phalloidin (ThermoFisher, A22284) was added at 1:100 in PBST. Larvae were
781 incubated for 4 h at room temperature and then washed 4 × 5 min in PBST. Larvae were mounted
782 on glass slides with Prolong Gold (ThermoFisher Scientific) using No. 1.5 coverslips. To image
783 hair bundle orientation and FM 1-43FX label in lateral-line hair cells, a Zeiss LSM780 confocal
784 microscope with Airyscan was used. Hair cells were imaged using a 63× 1.3 NA oil objective and
785 processed with an Airyscan processing factor of 7.0. For analysis, Z-stacks were max-projected in
786 FIJI. Images were background subtracted using a rolling ball correction. Hair cells with a FM 1-
787 43FX intensity more than twice the background intensity were scored as FM 1-43FX positive.
788

789 **Zebrafish Ca^{2+} imaging and behavior**

790 For imaging of mechanosensitive Ca^{2+} signals in neuromast hair bundles,
791 *Tg(myo6b:memGCaMP6s)* animals were mounted on their side on Sylgard chamber in E3 embryo
792 media containing 0.2% MESAB (Lukasz and Kindt, 2018). Larvae were then pinned and a solution
793 containing α-bungarotoxin (125 μM, Tocris) was injected into the heart cavity for paralysis during
794 imaging. After paralysis, larvae were immersed in extracellular imaging solution (in mM: 140

795 NaCl, 2 KCl, 2 $CaCl_2$, 1 $MgCl_2$ and 10 HEPES, pH 7.3, OSM 310 +/- 10). To image Ca^{2+} signals
796 in the hair bundles we used a Bruker Swept-Field confocal system equipped with a Rolera EM-C2
797 CCD camera (QImaging, Surrey, Canada) and a Nikon CFI Fluor 60×1.0 NA water immersion
798 objective as previously described (Q. Zhang et al., 2018). The system includes a band-pass 488/561
799 nm filter set (59904-ET, Chroma) and is controlled using Prairie View software (Bruker
800 Corporation). A piezoelectric motor (PICMA P-882.11-888.11 series, PI Instruments) attached to
801 the objective and used to acquire 5-plane Z-stacks every 0.5 µm using a 35 µm slit at a 50-Hz
802 frame rate for a 10-Hz volume rate. A fluid-jet composed of a glass capillary attached to a pressure
803 clamp system (HSPC-2-SB, ALA) was used to deliver a 500-ms anterior and posterior step
804 stimulation to deflect hair bundles along their axis of sensitivity.

805 To quantify GCaMP6s fluorescent intensity changes during stimulation, we registered the
806 Z-stacks and then average projected the Z-stacks into a single plane. We then loaded the projected
807 images into FIJI and used the Time Series Analyzer V3 plugin to create circular ROIs with a ~1.7
808 µm diameter. ROIs were placed on the center of each individual bundle. We then measured and
809 plotted change in the mean intensity ($\Delta F/F_0$) within the region during the recording period. The
810 mean intensity within each ROI was computed for each hair bundle. A hair bundle with a signal
811 magnitude (peak value of intensity change upon stimulation) above 10% $\Delta F/F_0$ was considered
812 mechanosensitive. To create the AVG hair bundle GCaMP6s ($\Delta F/F_0$) per neuromast plot in Figure
813 5-figure supplement 2C, only traces from mechanosensitive cells were averaged.

814 A Zantiks MWP behavioral system was used to examine startle responses. The Zantiks
815 system tracked and monitored behavioral responses via a built-in infrared camera at 30 frames per
816 second. A 12-well plate was used to house larvae during behavioral analysis. Each well was filled
817 with E3 and 1 larva. All fish were acclimated in the plate within the Zantiks chamber in dark for

818 15 min before each test. To induce startle, an integrated stepper motor was used to drive a
819 vibration-induced startle response. A vibrational stimulus that triggered a maximal % of animals
820 startling in controls without any tracking artifacts (due to the vibration) was used for our analyses.
821 Each larva was presented with the vibrational stimulus 5 times with 100 s between trials. During
822 the tracking and stimulation, a Cisco router connected to the Zantiks system was used to relay *x*, *y*
823 coordinates of each larva every frame. To qualify as a startle response, a distance above 4 pixels
824 or ~1.9 mm was required within 2 frames after stimulus onset. Animals were excluded from our
825 analysis if no tracking data was recorded for the animal.
826

827 **Zebrafish Statistics**

828 All data shown are mean ± standard error of the mean (SEM). All experiments were performed on
829 at least 4 animals and 8 neuromasts and 4 cristae. Behavior analysis and Ca^{2+} imaging was repeated
830 at least twice on two independent days. All statistical analysis was performed using GraphPad
831 Prism 8.0. A D'Agostino and Pearson test was used to test data for normality. A one-way ANOVA
832 with a Dunnett's correction for multiple comparisons was used to compare differences between
833 siblings and controls regarding the % of mechanosensitive hair cells, number of hair cells, % of
834 FM 1-43 positive hair cells, average FM 1-43 label. For proportion of animals startling and
835 comparisons for FM 1-43FX label, a Kruskal-Wallis test with a Dunnett's correction for multiple
836 comparisons was used.
837

838 **Expression and purification of bacterially expressed *hs* CIB2, CIB3, TMC1-IL1, and TMC1-**
839 **NT**

840 DNA sequences encoding for *hs* CIB2, CIB3, TMC1-IL1, and TMC1-NT were subcloned into
841 *NdeI* and *XhoI* sites of the pET21a vector. All DNA constructs were sequence verified. Protein
842 fragments were expressed in *Escherichia coli* BL21 Rosetta (DE3) (Novagen) cells, which were
843 cultured in LB or TB media, induced at OD_{600} ~0.4-0.6 with 1 mM IPTG and grown at 20°C or
844 30°C for ~16 h. Protein fragments for NMR were produced using the same cells cultured in M9
845 minimal media supplemented with MEM vitamin solution (Gibco) and 1g/L $^{15}NH_4Cl$ (Cambridge
846 Isotopes) to produce uniformly labeled [U-^{15}N] protein. Cells were lysed by sonication in
847 denaturing buffer (20 mM Tris HCl, pH 7.5, 6 M guanidine hydrochloride, 10 mM $CaCl_2$, and 20
848 mM imidazole) or non-denaturing buffer (20 mM Tris HCl, pH 7.5, and 20 mM imidazole for *hs*
849 TMC1-NT). The cleared lysates were loaded onto Ni-Sepharose (GE Healthcare) and eluted with
850 denaturing buffer or non-denaturing buffer supplemented with 500 mM imidazole. Denatured
851 proteins were refolded using MWCO 2,000 membranes (Spectra/Por 7) in dialysis buffer (400 mM
852 Arg-HCl, 20 mM Tris-HCl, pH 7.5, 150 mM KCl, 50 mM NaCl, 2 mM $CaCl_2$, 2 mM DTT) for
853 ~16 hr. Before starting refolding reactions (when applicable), elution solutions were diluted to
854 ~0.5 mg/mL using the denaturing buffer, and then reduced by using 2 mM DTT in the diluted
855 sample. Refolded and soluble proteins were concentrated using Vivaspin 20 or Amicon 15
856 centrifugal concentrators (10 kDa, 5 kDa, or 3 kDa molecular weight cutoff) and further purified
857 on Superdex S75 columns (GE Healthcare) in SEC buffer (50 mM HEPES, pH 7.5, 126 mM KCl,
858 10 mM NaCl, 3 mM $CaCl_2$, 5 mM DTT). Proteins were concentrated to ~0.5 mL for nuclear
859 magnetic resonance (NMR) experiments.
860
861 **NMR**

862 Purified NMR samples were at concentrations of ~1.4 mM, ~0.2 mM, ~0.8 mM, and ~0.2 mM for
863 CIB2, CIB3, CIB2 + TMC1-IL1, and CIB3 + TMC1-IL1, respectively, in SEC buffer (50 mM
864 HEPES, pH 7.5, 126 mM KCl, 10 mM NaCl, 3 mM $CaCl_2$, 5 mM DTT), supplemented with 10%
865 (v/v) D_2O and 0.2 mM 2,2-dimethyl-2-silapentane-5-sulphonate (DSS) for field-frequency locking
866 and chemical shift referencing. Two-dimensional ^{1}H-^{15}N TROSY-HSQC spectra (Nietlispach,
867 2005) were recorded for each sample at 25°C on a Bruker Avance III HD 800 MHz spectrometer
868 equipped with a 5 mm TXI cryoprobe with z-gradients. Data were collected using 20 to 24 scans,
869 2,048 x 280 datapoints, and spectral widths of 17482.518 x 4054.298 Hz in the ^{1}H and ^{15}N
870 dimensions, respectively. Data were processed and visualized using NMRFx (Norris et al., 2016).
871

872 **Simulated Systems**

873 Models for monomeric *hs* TMC1 (residues 84 to 760; NCBI ID: NP_619636.2) and *hs* TMC2 (148
874 to 863; NCBI ID: NP_542789.2) in complex with full-length *hs* CIB2 (NCBI ID: NP_006374.1)
875 and *hs* CIB3 (NCBI ID: NP_473454.1), as well as truncated dimeric models of *hs* TMC1 (residues
876 260 to 760; NCBI ID: NP_619636.2) and *hs* TMC2 (residues 324 to 863; NCBI ID: NP_542789.2)
877 were generated using AF2 (Evans et al., 2021; Jumper et al., 2021). The TMC2 C-terminal end
878 (residues 818 to 863) was truncated to match the C-terminal end of TMC1. Using VMD
879 (Humphrey et al., 1996), a model of dimeric *hs* TMC1 + *hs* CIB3-Ca^{2+} was constructed by aligning
880 the monomeric *hs* TMC1 + *hs* CIB3 complex to the transmembrane region of the truncated dimeric
881 *hs* TMC1 model. Coordinates for Ca^{2+} ions were obtained by aligning the crystal structure of Mg^{2+}-
882 bound *hs* CIB3 in complex with a *hs* TMC1-IL1 peptide (PDB code: 6WUD) (Liang et al., 2021)
883 to the AF2 model of monomeric *hs* TMC1 + *hs* CIB3, then manually changing Mg^{2+} for Ca^{2+}. This
884 model was minimized for 1,000 steps in vacuum using NAMD (Phillips et al., 2005) and the

885 CHARMM36 force field (Best et al., 2012; Huang and MacKerell, 2014; Vanommeslaeghe and
886 MacKerell, 2015) and served as a reference model for aligning other combinations of *hs* TMC1 or
887 *hs* TMC2 with *hs* CIB2 or *hs* CIB3. All models were either embedded into pure POPC or mixed
888 membrane lipid bilayers using CHARMM-GUI (Jo et al., 2009, 2008, 2007; Lee et al., 2019) as
889 summarized in Table supplement 1. The mixed membrane mimicked stereocilia membrane
890 composition (Zhao et al., 2012). The protein-lipid system was then solvated using TIP3P explicit
891 water and neutralized with 0.150 M KCl, representative of endolymph ionic concentration (Bosher
892 and Warren, 1978).
893
894 **Simulations using NAMD**
895 All-atom MD simulations were performed and analyzed using NAMD 2.13 (Phillips et al., 2005)
896 and the CHARMM36 force field with CMAP corrections (Best et al., 2012; Huang and MacKerell,
897 2014; Vanommeslaeghe and MacKerell, 2015). For all systems, equilibrium simulations consisted
898 of 2,000 steps of minimization, 0.5 ns of dynamics with everything excluding lipid tails
899 fixed/constrained, 0.5 ns of dynamics with harmonic constraints applied to the protein (1 kcal mol^{-}
900 ^{1} Å^{-2}), 1 ns of free dynamics in the *NpT* ensemble (γ = 1 ps^{-1}), and up to 100 ns of free dynamics
901 in the *NpT* ensemble (γ = 0.1 ps^{-1}) prior to non-equilibrium production runs. A piston period of
902 200 fs and a damping timescale of 50 fs was used for pressure control and atomic coordinates were
903 saved every 5 ps. All simulations were performed at 310 K and 1 atmosphere of pressure by using
904 the Langevin thermostat and Nosé-Hoover Langevin pressure control. A 12-Å cutoff distance was
905 employed with a force-based switching function starting at 10 Å. Periodic boundary conditions
906 and the PME method were used to calculate long-range electrostatic interactions with a grid
907 density greater than 1 Å^{-3}. An integration timestep of 2 fs with electrostatic interactions computed

908 every other timestep was utilized for every simulation in tandem with the SHAKE algorithm for
909 the constraint of hydrogen atoms. A constant electric field was applied to all atoms in non-
910 equilibrium simulations with transmembrane potential (Gumbart et al., 2012).
911
912 **Simulations using Anton 2**
913 We used Anton 2, a massively parallel special purpose machine for MD simulations (Shaw et al.,
914 2014), to run simulations of *hs* TMC1 + *hs* CIB2-Ca^{2+} in POPC (simulations S1d-g; Table
915 supplement 1), *hs* TMC1 + *hs* CIB2 in POPC (simulations S2d-2g; Table supplement 1), *hs* TMC1
916 in POPC (simulations S3d-g; Table supplement 1), and *hs* TMC1 + *hs* CIB2 in a mixed membrane
917 (simulations S4c-d; Table supplement 1). Coordinates of the pre-equilibrated systems were
918 converted to an Anton 2 compatible dms file format using the NAMDtoDMS.py script provided
919 by the Pittsburgh Supercomputing Center. Simulations used CHARMM36 forcefields and were
920 performed in the *NpT* ensemble (310 K, 1 atm) using the multigrator integration framework
921 (Lippert et al., 2013) with a 2.5 fs integration timestep and saved every 120 ps. The MTK barostat
922 and Nosé-Hoover thermostat was updated every 480 and 24 steps, respectively. Semi-isotropic
923 pressure coupling was used. Long range electrostatic interactions were calculated using u-series
924 electrostatics with a 64 × 64 × 64 grid. Van der Waals interactions were calculated with a cutoff
925 of 12 Å. Transmembrane voltages were generated by applying a constant electric field to all atoms
926 (Gumbart et al., 2012).
927
928 **Simulation analysis procedures and tools**
929 BSA was computed in VMD by measuring SASA for both TMC and CIB monomers, then
930 subtracting SASA for the complex. BSA for interacting molecules A and B were computed as

931 $BSA_{AB} = 1/2(SASA_A + SASA_B - SASA_{AB})$. RMSD values were computed in VMD using Cα
932 atoms and initial models as references, with alignments carried out using the corresponding
933 subdomains when indicated. VMD was used to analyze trajectories, render molecular images, and
934 create videos. Xmgrace and gnuplot were used to generate plots. Sequences for CIB and TMC
935 isoforms from various species were obtained from the NCBI protein database. Sequences were
936 aligned utilizing the MUSCLE algorithm within Geneious (Kearse et al., 2012). Aligned sequences
937 were loaded into JalView (Waterhouse et al., 2009) and colored based on a sequence identity
938 threshold of 45%. Ionic currents were computed by counting the number of crossing, with
939 conductance values estimated as in Walujkar et al., 2021.
940
941 **<u>Resource Availability</u>**
942 **Lead Contact**
943 Further information and requests for resources and reagents should be directed to the Lead
944 Contacts, Drs. Marcos Sotomayor (sotomayor@uchicago.edu) and Zubair M. Ahmed
945 (zmahmed@som.umaryland.edu).
946
947 **Materials availability**
948 Materials generated in this study, including strains, plasmids and clones, are freely available from
949 the Lead Contact upon request.
950
951 **Data and code availability**
952 This study did not generate any unique datasets or code.
953

954 **Acknowledgements**

955 We acknowledge Sakina Rehman for assistance with animal work, Neal Taliwal for assistance
956 with molecular cloning, Chunhua Yuan for assistance with initial nuclear magnetic resonance
957 experiments, and Collin R. Nisler and Harsha Mandayam Bharathi for assistance with simulations
958 analyses. Simulations were carried out at the Ohio Supercomputer Center (OSC grants PAS1037
959 and PAA0217) and the Pittsburgh Supercomputer Center (PSC Anton 2 grant MCB150024P).
960 Nuclear magnetic resonance data were acquired at the Ohio State University Campus Chemical
961 Instrument Center. This study was supported by NIH/NIDCD grants R01DC015271 to M.S. and
962 R01DC012564 to Z.M.A. and G.I.F., an Intramural Research Program Grant 1ZIADC000085-01
963 to K.S.K., and NIH grants UF1NS111695, R01DC018304, R01DC002390, R01DC018061 to
964 K.E.C.

965

966 **Additional information**

967 **Author contributions**

968 Z.M.A., K.S.K., and M.S. conceived the studies. A.P.J.G. carried out all audiometric recordings
969 in mice, immunolocalization studies, cochlear and vestibular explant cultures, FM 1-43 uptake
970 experiment on mouse tissues, RT-qPCRs, exploratory testing, *Cib2* and *Cib3* mouse phenotyping
971 and genotyping, cloning of CIB2 and CIB3 in pET21a vectors. K.S.K. conducted zebrafish FM 1-
972 43, FM 4-64, FM 1-43FX labeling, Ca^{2+} imaging and immunostaining. A.J.B. created the *cib2* and
973 *cib3* zebrafish mutants. R.A.R. did the zebrafish behavioral studies. W-H.W. did the cloning and
974 mutagenesis of CIB and TMC constructs, protein expression and purification for NMR
975 experiments, as well as model building and molecular dynamics simulations. J.S.M. did NMR
976 experiments and NMR data processing. E.M.R. performed FM 1-43 uptake experiments in mice.

J.M.L. and S.W. did model building. M.P.F. supervised NMR experiments and project. M.S. supervised project and assisted with cloning, strategies for protein refolding, model building, and simulations. H.H.V.C. and O.A.Z. performed VOR, OKN measurements and vestibular function evaluation of mice. J.R.H., analyzed the mouse FM 1-43 experiments data, provided supervision and resources. S.R., and Z.M.A., supervised the project, reviewed and interpreted the results, provided resources. All authors contributed to data analysis. A.P.J.G., W-H. W., K.S.K., K.C., M.S. and Z.M.A. wrote the manuscript. All authors edited the manuscript and approved for submission.

985 **References**

986 Ahmed ZM, Goodyear R, Riazuddin Saima, Lagziel A, Legan PK, Behra M, Burgess SM, Lilley
987 KS, Wilcox ER, Riazuddin Sheikh, Griffith AJ, Frolenkov GI, Belyantseva IA, Richardson
988 GP, Friedman TB. 2006. The tip-link antigen, a protein associated with the transduction
989 complex of sensory hair cells, is protocadherin-15. *J Neurosci* **26**:7022–7034.
990 doi:10.1523/JNEUROSCI.1163-06.2006

991 Akyuz N, Karavitaki KD, Pan B, Tamvakologos PI, Brock KP, Li Y, Marks DS, Corey DP.
992 2022. Mechanical gating of the auditory transduction channel TMC1 involves the fourth
993 and sixth transmembrane helices. *Sci Adv* **8**:eabo1126. doi:10.1126/sciadv.abo1126

994 Baek S, Tran NTT, Diaz DC, Tsai Y-Y, Acedo JN, Lush ME, Piotrowski T. 2022. Single-cell
995 transcriptome analysis reveals three sequential phases of gene expression during zebrafish
996 sensory hair cell regeneration. *Dev Cell* **57**:799-819.e6.
997 doi:10.1016/J.DEVCEL.2022.03.001

998 Ballesteros A, Fenollar-Ferrer C, Swartz KJ. 2018. Structural relationship between the putative
999 hair cell mechanotransduction channel TMC1 and TMEM16 proteins. *Elife* **7**.
1000 doi:10.7554/eLife.38433

1001 Beraneck M, Cullen KE. 2007. Activity of vestibular nuclei neurons during vestibular and
1002 optokinetic stimulation in the alert mouse. *J Neurophysiol* **98**:1549–1565.
1003 doi:10.1152/jn.00590.2007

1004 Beraneck M, McKee JL, Aleisa M, Cullen KE. 2008. Asymmetric recovery in cerebellar-
1005 deficient mice following unilateral labyrinthectomy. *J Neurophysiol* **100**:945–958.
1006 doi:10.1152/jn.90319.2008

1007 Best RB, Zhu X, Shim J, Lopes PE, Mittal J, Feig M, Mackerell Jr. AD. 2012. Optimization of
1008 the additive CHARMM all-atom protein force field targeting improved sampling of the
1009 backbone phi, psi and side-chain chi(1) and chi(2) dihedral angles. *J Chem Theory Comput*
1010 **8**:3257–3273. doi:10.1021/ct300400x

1011 Beurg M, Cui R, Goldring AC, Ebrahim S, Fettiplace R, Kachar B. 2018. Variable number of
1012 TMC1-dependent mechanotransducer channels underlie tonotopic conductance gradients in
1013 the cochlea. *Nat Commun* **9**:2185. doi:10.1038/s41467-018-04589-8

1014 Beurg M, Fettiplace R, Nam J-H, Ricci AJ. 2009. Localization of inner hair cell
1015 mechanotransducer channels using high-speed calcium imaging. *Nat Neurosci* **12**:553–558.
1016 doi:10.1038/nn.2295

1017 Beurg M, Nam J-H, Fettiplace R. 2021. The speed of the hair cell mechanotransducer channel
1018 revealed by fluctuation analysis. *J Gen Physiol* **153**. doi:10.1085/jgp.202112959

1019 Blazejczyk M, Sobczak A, Debowska K, Wisniewska MB, Kirilenko A, Pikula S, Jaworski J,
1020 Kuznicki J, Wojda U. 2009. Biochemical characterization and expression analysis of a
1021 novel EF-hand Ca2+ binding protein calmyrin2 (Cib2) in brain indicates its function in
1022 NMDA receptor mediated Ca2+ signaling. *Arch Biochem Biophys* **487**:66–78.
1023 doi:10.1016/j.abb.2009.05.002

1024 Booth KT, Kahrizi K, Babanejad M, Daghagh H, Bademci G, Arzhangi S, Zareabdollahi D,
1025 Duman D, El-Amraoui A, Tekin M, Najmabadi H, Azaiez H, Smith RJ. 2018. Variants in
1026 CIB2 cause DFNB48 and not USH1J. *Clin Genet* **93**:812–821. doi:10.1111/cge.13170

1027 Bosher SK, Warren RL. 1978. Very low calcium content of cochlear endolymph, an extracellular
1028 fluid. *Nature* **273**:377–378. doi:10.1038/273377a0

1029 Chen Z, Zhu S, Kindig K, Wang S, Chou SW, Davis RW, Dercoli MR, Weaver H, Stepanyan R,
1030 McDermott BM. 2020. Tmc proteins are essential for zebrafish hearing where Tmc1 is not
1031 obligatory. *Hum Mol Genet* **29**:2004–2021. doi:10.1093/HMG/DDAA045

1032 Chou SW, Chen Z, Zhu S, Davis RW, Hu J, Liu L, Fernando CA, Kindig K, Brown WC,
1033 Stepanyan R, McDermott BM. 2017. A molecular basis for water motion detection by the
1034 mechanosensory lateral line of zebrafish. *Nat Commun* **8**. doi:10.1038/s41467-017-01604-2

1035 Cullen KE. 2019. Vestibular processing during natural self-motion: implications for perception
1036 and action. *Nat Rev Neurosci* **20**:346–363. doi:10.1038/s41583-019-0153-1

1037 Cunningham CL, Qiu X, Wu Z, Zhao B, Peng G, Kim YH, Lauer A, Müller U. 2020. TMIE
1038 Defines Pore and Gating Properties of the Mechanotransduction Channel of Mammalian
1039 Cochlear Hair Cells. *Neuron* **107**:126-143.e8. doi:10.1016/j.neuron.2020.03.033

1040 Dal Cortivo G, Marino V, Iacobucci C, Vallone R, Arlt C, Rehkamp A, Sinz A, Dell'Orco D.
1041 2019. Oligomeric state, hydrodynamic properties and target recognition of human Calcium
1042 and Integrin Binding protein 2 (CIB2). *Sci Rep* **9**. doi:10.1038/s41598-019-51573-3

1043 Effertz T, Becker L, Peng AW, Ricci AJ. 2017. Phosphoinositol-4,5-bisphosphate regulates
1044 auditory hair-cell mechanotransduction-channel pore properties and fast adaptation. *J*
1045 *Neurosci* **37**:11632–11646. doi:10.1523/JNEUROSCI.1351-17.2017

1046 Erickson T, Morgan CP, Olt J, Hardy K, Busch-Nentwich E, Maeda R, Clemens R, Krey JF,
1047 Nechiporuk A, Barr-Gillespie PG, Marcotti W, Nicolson T. 2017. Integration of Tmc1/2
1048 into the mechanotransduction complex in zebrafish hair cells is regulated by
1049 Transmembrane O-methyltransferase (Tomt). *Elife* **6**. doi:10.7554/eLife.28474

1050 Erickson T, Pacentine I V, Venuto A, Clemens R, Nicolson T. 2019. The lhfpl5 Ohnologs
1051 lhfpl5a and lhfpl5b Are Required for Mechanotransduction in Distinct Populations of
1052 Sensory Hair Cells in Zebrafish. *Front Mol Neurosci* **12**:320.
1053 doi:10.3389/fnmol.2019.00320

1054 Ernest S, Rauch GJ, Haffter P, Geisler R, Petit C, Nicolson T. 2000. Mariner is defective in
1055 myosin VIIA: A zebrafish model for human hereditary deafness. *Hum Mol Genet* **9**:2189–
1056 2196. doi:10.1093/hmg/9.14.2189

1057 Evans R, O'Neill M, Pritzel A, Antropova N, Senior A, Green T, Žídek A, Bates R, Blackwell S,
1058 Yim J, Ronneberger O, Bodenstein S, Zielinski M, Bridgland A, Potapenko A, Cowie A,
1059 Tunyasuvunakool K, Jain R, Clancy E, Kohli P, Jumper J, Hassabis D. 2021. Protein
1060 complex prediction with AlphaFold-Multimer. *bioRxiv* 2021.10.04.463034.
1061 doi:10.1101/2021.10.04.463034

1062 Fettiplace R. 2017. Hair cell transduction, tuning, and synaptic transmission in the mammalian
1063 cochlea. *Compr Physiol* **7**:1197–1227. doi:10.1002/cphy.c160049

1064 Fettiplace R, Furness DN, Beurg M. 2022. The conductance and organization of the TMC1-
1065 containing mechanotransducer channel complex in auditory hair cells. *Proc Natl Acad Sci U*
1066 *S A* **119**:e2210849119. doi:10.1073/pnas.2210849119

1067 Frolenkov GI, Belyantseva IA, Friedman TB, Griffith AJ. 2004. Genetic insights into the
1068 morphogenesis of inner ear hair cells. *Nat Rev Genet* **5**:489–498. doi:10.1038/nrg1377

1069 Giese APJ, Tang YQ, Sinha GP, Bowl MR, Goldring AC, Parker A, Freeman MJ, Brown SDM,
1070 Riazuddin S, Fettiplace R, Schafer WR, Frolenkov GI, Ahmed ZM. 2017. CIB2 interacts
1071 with TMC1 and TMC2 and is essential for mechanotransduction in auditory hair cells. *Nat*

1072 *Commun* **8**. doi:10.1038/s41467-017-00061-1

1073 Gillespie PG, Müller U. 2009. Mechanotransduction by hair cells: models, molecules, and
1074 mechanisms. *Cell* **139**:33–44. doi:10.1016/j.cell.2009.09.010

1075 Gleason MR, Nagiel A, Jamet S, Vologodskaia M, López-Schier H, Hudspeth AJ. 2009. The
1076 transmembrane inner ear (Tmie) protein is essential for normal hearing and balance in the
1077 zebrafish. *Proc Natl Acad Sci U S A* **106**:21347–52. doi:10.1073/pnas.0911632106

1078 Gopal SR, Chen DHC, Chou SW, Zang J, Neuhauss SCF, Stepanyan R, McDermott BM,
1079 Alagramam KN. 2015. Zebrafish models for the mechanosensory hair cell dysfunction in
1080 usher syndrome 3 reveal that Clarin-1 is an essential hair bundle protein. *J Neurosci*
1081 **35**:10188–10201. doi:10.1523/JNEUROSCI.1096-15.2015

1082 Gumbart J, Khalili-Araghi F, Sotomayor M, Roux B. 2012. Constant electric field simulations of
1083 the membrane potential illustrated with simple systems. *Biochim Biophys Acta - Biomembr*
1084 **1818**:294–302. doi:10.1016/j.bbamem.2011.09.030

1085 Huang H, Bogstie JN, Vogel HJ. 2012. Biophysical and structural studies of the human calcium-
1086 and integrin-binding protein family: Understanding their functional similarities and
1087 differences. *Biochem Cell Biol* **90**:646–656. doi:10.1139/o2012-021

1088 Huang J, MacKerell ADJ. 2014. CHARMM36 all-atom additive protein force field: Validation
1089 based on comparison to NMR data. *J Comput Chem* **34**:2135–2145.
1090 doi:10.1002/jcc.23354.CHARMM36

1091 Humphrey W, Dalke A, Schulten K. 1996. VMD: Visual molecular dynamics. *J Mol Graph*
1092 **14**:33–38. doi:10.1016/0263-7855(96)00018-5

1093 Jeong H, Clark S, Goehring A, Dehghani-Ghahnaviyeh S, Rasouli A, Tajkhorshid E, Gouaux E.
1094 2022. Structures of the TMC-1 complex illuminate mechanosensory transduction. *Nature*
1095 **610**:796–803. doi:10.1038/s41586-022-05314-8

1096 Jiang T, Kindt K, Wu DK. 2017. Transcription factor emx2 controls stereociliary bundle
1097 orientation of sensory hair cells. *Elife* **6**:1–26. doi:10.7554/eLife.23661

1098 Jo S, Kim T, Im W. 2007. Automated builder and database of protein/membrane complexes for
1099 molecular dynamics simulations. *PLoS One* **2**. doi:10.1371/journal.pone.0000880

1100 Jo S, Kim T, Iyer VG, Im W. 2008. CHARMM-GUI: A web-based graphical user interface for
1101 CHARMM. *J Comput Chem* **29**:1859–1865. doi:10.1002/jcc.20945

1102 Jo S, Lim JB, Klauda JB, Im W. 2009. CHARMM-GUI membrane builder for mixed bilayers
1103 and its application to yeast membranes. *Biophys J* **97**:50–58. doi:10.1016/j.bpj.2009.04.013

1104 Jojoa-Cruz S, Saotome K, Murthy SE, Tsui CCA, Sansom MS, Patapoutian A, Ward AB. 2018.
1105 Cryo-EM structure of the mechanically activated ion channel OSCA1.2. *Elife* **7**.
1106 doi:10.7554/eLife.41845

1107 Jumper J, Evans R, Pritzel A, Green T, Figurnov M, Ronneberger O, Tunyasuvunakool K, Bates
1108 R, Žídek A, Potapenko A, Bridgland A, Meyer C, Kohl SAA, Ballard AJ, Cowie A,
1109 Romera-Paredes B, Nikolov S, Jain R, Adler J, Back T, Petersen S, Reiman D, Clancy E,
1110 Zielinski M, Steinegger M, Pacholska M, Berghammer T, Bodenstein S, Silver D, Vinyals
1111 O, Senior AW, Kavukcuoglu K, Kohli P, Hassabis D. 2021. Highly accurate protein
1112 structure prediction with AlphaFold. *Nature* 1–11. doi:10.1038/s41586-021-03819-2

1113 Karplus M, Petsko GA. 1990. Molecular dynamics simulations in biology. *Nature* **347**:631–9.

1114 doi:10.1038/347631a0

1115 Kawashima Y, Géléoc GSG, Kurima K, Labay V, Lelli A, Asai Y, Makishima T, Wu DK, Della
1116 Santina CC, Holt JR, Griffith AJ. 2011. Mechanotransduction in mouse inner ear hair cells
1117 requires transmembrane channel-like genes. *J Clin Invest* **121**:4796–809.
1118 doi:10.1172/JCI60405

1119 Kawashima Y, Kurima K, Pan B, Griffith AJ, Holt JR. 2015. Transmembrane channel-like
1120 (TMC) genes are required for auditory and vestibular mechanosensation. *Pflügers Arch -*
1121 *Eur J Physiol* **467**:85–94. doi:10.1007/s00424-014-1582-3

1122 Kazmierczak P, Sakaguchi H, Tokita J, Wilson-Kubalek EM, Milligan RA, Müller U, Kachar B.
1123 2007. Cadherin 23 and protocadherin 15 interact to form tip-link filaments in sensory hair
1124 cells. *Nature* **449**:87–91. doi:10.1038/nature06091

1125 Kearse M, Moir R, Wilson A, Stones-Havas S, Cheung M, Sturrock S, Buxton S, Cooper A,
1126 Markowitz S, Duran C, Thierer T, Ashton B, Meintjes P, Drummond A. 2012. Geneious
1127 Basic: an integrated and extendable desktop software platform for the organization and
1128 analysis of sequence data. *Bioinformatics* **28**:1647–9. doi:10.1093/bioinformatics/bts199

1129 Kim KX, Beurg M, Hackney CM, Furness DN, Mahendrasingam S, Fettiplace R. 2013. The role
1130 of transmembrane channel–like proteins in the operation of hair cell mechanotransducer
1131 channels. *J Gen Physiol* **142**:493–505. doi:10.1085/jgp.201311068

1132 Kindig K, Stepanyan R, Kindt KS, McDermott BM. 2023. Asymmetric mechanotransduction by
1133 hair cells of the zebrafish lateral line. *Curr Biol* **33**:1295-1307.e3.
1134 doi:10.1016/j.cub.2023.02.033

1135 Lee Jumin, Patel DS, Ståhle J, Park SJ, Kern NR, Kim S, Lee Joonseong, Cheng X, Valvano
1136 MA, Holst O, Knirel YA, Qi Y, Jo S, Klauda JB, Widmalm G, Im W. 2019. CHARMM-
1137 GUI Membrane Builder for Complex Biological Membrane Simulations with Glycolipids
1138 and Lipoglycans. *J Chem Theory Comput* **15**:775–786. doi:10.1021/acs.jctc.8b01066

1139 Liang X, Qiu X, Dionne G, Cunningham CL, Pucak ML, Peng G, Kim YH, Lauer A, Shapiro L,
1140 Müller U. 2021. CIB2 and CIB3 are auxiliary subunits of the mechanotransduction channel
1141 of hair cells. *Neuron*. doi:10.1016/j.neuron.2021.05.007

1142 Lippert R a, Predescu C, Ierardi DJ, Mackenzie KM, Eastwood MP, Dror RO, Shaw DE. 2013.
1143 Accurate and efficient integration for molecular dynamics simulations at constant
1144 temperature and pressure. *J Chem Phys* **139**:164106. doi:10.1063/1.4825247

1145 Liu X, Wang J, Sun L. 2018. Structure of the hyperosmolality-gated calcium-permeable channel
1146 OSCA1.2. *Nat Commun* **9**:5060. doi:10.1038/s41467-018-07564-5

1147 López-Schier H, Hudspeth AJ. 2006. A two-step mechanism underlies the planar polarization of
1148 regenerating sensory hair cells. *Proc Natl Acad Sci U S A* **103**:18615–18620.
1149 doi:10.1073/pnas.0608536103

1150 Lukasz D, Kindt KS. 2018. In vivo calcium imaging of lateral-line hair cells in larval zebrafish. *J*
1151 *Vis Exp* **2018**:1–14. doi:10.3791/58794

1152 Maeda R, Kindt KS, Mo W, Morgan CP, Erickson T, Zhao H, Clemens-Grisham R, Barr-
1153 Gillespie PG, Nicolson T. 2014. Tip-link protein protocadherin 15 interacts with
1154 transmembrane channel-like proteins TMC1 and TMC2. *Proc Natl Acad Sci U S A*
1155 **111**:12907–12. doi:10.1073/pnas.1402152111

1156 Maeda R, Pacentine I V., Erickson T, Nicolson T. 2017. Functional analysis of the
1157 transmembrane and cytoplasmic domains of Pcdh15a in zebrafish hair cells. *J Neurosci*
1158 2216–16. doi:10.1523/JNEUROSCI.2216-16.2017

1159 McInturff S, Burns JC, Kelley MW. 2018. Characterization of spatial and temporal development
1160 of Type I and Type II hair cells in the mouse utricle using new cell-type-specific markers.
1161 *Biol Open* **7**:1–13. doi:10.1242/bio.038083

1162 Meyers JR, MacDonald RB, Duggan A, Lenzi D, Standaert DG, Corwin JT, Corey DP. 2003.
1163 Lighting up the Senses: FM1-43 Loading of Sensory Cells through Nonselective Ion
1164 Channels. *J Neurosci* **23**:4054–4065. doi:10.1523/JNEUROSCI.23-10-04054.2003

1165 Michel V, Booth KT, Patni P, Cortese M, Azaiez H, Bahloul A, Kahrizi K, Labbé M, Emptoz A,
1166 Lelli A, Dégardin J, Dupont T, Aghaie A, Oficjalska-Pham D, Picaud S, Najmabadi H,
1167 Smith RJ, Bowl MR, Brown SD, Avan P, Petit C, El-Amraoui A. 2017. CIB2, defective in
1168 isolated deafness, is key for auditory hair cell mechanotransduction and survival. *EMBO*
1169 *Mol Med* **9**:1711–1731. doi:10.15252/emmm.201708087

1170 Naz S, Giguere CM, Kohrman DC, Mitchem KL, Riazuddin Saima, Morell RJ, Ramesh A,
1171 Srisailpathy S, Deshmukh D, Riazuddin Sheikh, Griffith AJ, Friedman TB, Smith RJH,
1172 Wilcox ER. 2002. Mutations in a novel gene, TMIE, are associated with hearing loss linked
1173 to the DFNB6 locus. *Am J Hum Genet* **71**:632–636. doi:10.1086/342193

1174 Nicolson T. 2017. The genetics of hair-cell function in zebrafish. *J Neurogenet*.
1175 doi:10.1080/01677063.2017.1342246

1176 Nicolson T, Rüsch A, Friedrich RW, Granato M, Ruppersberg JP, Nüsslein-Volhard C. 1998.
1177 Genetic analysis of vertebrate sensory hair cell mechanosensation: The zebrafish circler

1178 mutants. *Neuron* **20**:271–283. doi:10.1016/S0896-6273(00)80455-9

1179 Nietlispach D. 2005. Suppression of anti-TROSY lines in a sensitivity enhanced gradient
1180 selection TROSY scheme. *J Biomol NMR* **31**:161–6. doi:10.1007/s10858-004-8195-7

1181 Norris M, Fetler B, Marchant J, Johnson BA. 2016. NMRFx Processor: a cross-platform NMR
1182 data processing program. *J Biomol NMR* **65**:205–216. doi:10.1007/s10858-016-0049-6

1183 Pacentine I V, Nicolson T. 2019. Subunits of the mechano-electrical transduction channel,
1184 Tmc1/2b, require Tmie to localize in zebrafish sensory hair cells. *PLoS Genet* **15**:e1007635.
1185 doi:10.1371/journal.pgen.1007635

1186 Pan B, Akyuz N, Liu X-P, Asai Y, Nist-Lund C, Kurima K, Derfler BH, György B, Limapichat
1187 W, Walujkar S, Wimalasena LN, Sotomayor M, Corey DP, Holt JR. 2018. TMC1 Forms
1188 the Pore of Mechanosensory Transduction Channels in Vertebrate Inner Ear Hair Cells.
1189 *Neuron* **99**:736-753.e6. doi:10.1016/j.neuron.2018.07.033

1190 Pan B, Géléoc GS, Asai Y, Horwitz GC, Kurima K, Ishikawa K, Kawashima Y, Griffith AJ, Holt
1191 JR. 2013. TMC1 and TMC2 are components of the mechanotransduction channel in hair
1192 cells of the mammalian inner ear. *Neuron* **79**:504–15. doi:10.1016/j.neuron.2013.06.019

1193 Phillips JB, Blanco-Sanchez B, Lentz JJ, Tallafuss A, Khanobdee K, Sampath S, Jacobs ZG, Han
1194 PF, Mishra M, Titus TA, Williams DS, Keats BJ, Washbourne P, Westerfield M. 2011.
1195 Harmonin (Ush1c) is required in zebrafish Müller glial cells for photoreceptor synaptic
1196 development and function. *DMM Dis Model Mech* **4**:786–800. doi:10.1242/dmm.006429

1197 Phillips JC, Braun R, Wang W, Gumbart J, Tajkhorshid E, Villa E, Chipot C, Skeel RD, Kalé L,
1198 Schulten K. 2005. Scalable molecular dynamics with NAMD. *J Comput Chem* **26**:1781–

1802. doi:10.1002/jcc.20289

Pujol-Martí J, López-Schier H. 2013. Developmental and architectural principles of the lateral-line neural map. *Front Neural Circuits* **7**:1–9. doi:10.3389/fncir.2013.00047

Qiu X, Liang X, Llongueras JP, Cunningham C, Müller U. 2023. The tetraspan LHFPL5 is critical to establish maximal force sensitivity of the mechanotransduction channel of cochlear hair cells. *Cell Rep* **42**:112245. doi:10.1016/j.celrep.2023.112245

Riazuddin Saima, Belyantseva IA, Giese APJ, Lee K, Indzhykulian AA, Nandamuri SP, Yousaf R, Sinha GP, Lee S, Terrell D, Hegde RS, Ali RA, Anwar S, Andrade-Elizondo PB, Sirmaci A, Parise L V., Basit S, Wali A, Ayub M, Ansar M, Ahmad W, Khan SN, Akram J, Tekin M, Riazuddin Sheikh, Cook T, Buschbeck EK, Frolenkov GI, Leal SM, Friedman TB, Ahmed ZM. 2012. Alterations of the CIB2 calcium-and integrin-binding protein cause Usher syndrome type 1J and nonsyndromic deafness DFNB48. *Nat Genet* **44**:1265–1271. doi:10.1038/ng.2426

Seco CZ, Giese AP, Shafique S, Schraders M, Oonk AMM, Grossheim M, Oostrik J, Strom T, Hegde R, Van Wijk E, Frolenkov GI, Azam M, Yntema HG, Free RH, Riazuddin S, Verheij JBGM, Admiraal RJ, Qamar R, Ahmed ZM, Kremer H. 2016. Novel and recurrent CIB2 variants, associated with nonsyndromic deafness, do not affect calcium buffering and localization in hair cells. *Eur J Hum Genet* **24**:542–549. doi:10.1038/ejhg.2015.157

Seiler C, Ben-David O, Sidi S, Hendrich O, Rusch A, Burnside B, Avraham KB, Nicolson T. 2004. Myosin VI is required for structural integrity of the apical surface of sensory hair cells in zebrafish. *Dev Biol* **272**:328–338. doi:10.1016/j.ydbio.2004.05.004

Shaw DE, Grossman JP, Bank JA, Batson B, Butts JA, Chao JC, Deneroff MM, Dror RO, Even

1221 A, Fenton CH, Forte A, Gagliardo J, Gill G, Greskamp B, Ho CR, Ierardi DJ, Iserovich L,
1222 Kuskin JS, Larson RH, Layman T, Lee L-S, Lerer AK, Li C, Killebrew D, Mackenzie KM,
1223 Mok SY-H, Moraes MA, Mueller R, Nociolo LJ, Peticolas JL, Quan T, Ramot D, Salmon
1224 JK, Scarpazza DP, Schafer U Ben, Siddique N, Snyder CW, Spengler J, Tang PTP,
1225 Theobald M, Toma H, Towles B, Vitale B, Wang SC, Young C. 2014. Anton 2: Raising the
1226 Bar for Performance and Programmability in a Special-Purpose Molecular Dynamics
1227 SupercomputerSC14: International Conference for High Performance Computing,
1228 Networking, Storage and Analysis. IEEE. pp. 41–53. doi:10.1109/SC.2014.9

1229 Sheets L, He XJ, Olt J, Schreck M, Petralia RS, Wang YX, Zhang Q, Beirl A, Nicolson T,
1230 Marcotti W, Trapani JG, Kindt KS. 2017. Enlargement of ribbons in zebrafish hair cells
1231 increases calcium currents but disrupts afferent spontaneous activity and timing of stimulus
1232 onset. *J Neurosci* **37**:6299–6313. doi:10.1523/JNEUROSCI.2878-16.2017

1233 Shi T, Beaulieu MO, Saunders LM, Fabian P, Trapnell C, Segil N, Crump JG, Raible DW. 2023.
1234 Single-cell transcriptomic profiling of the zebrafish inner ear reveals molecularly distinct
1235 hair cell and supporting cell subtypes. *Elife* **12**:1–24. doi:10.7554/eLife.82978

1236 Siemens J, Lillo C, Dumont R a, Reynolds A, Williams DS, Gillespie PG, Müller U. 2004.
1237 Cadherin 23 is a component of the tip link in hair-cell stereocilia. *Nature* **428**:950–955.
1238 doi:10.1038/nature02483

1239 Smith ET, Pacentine I, Shipman A, Hill M, Nicolson T. 2020. Disruption of tmc1/2a/2b Genes in
1240 Zebrafish Reveals Subunit Requirements in Subtypes of Inner Ear Hair Cells. *J Neurosci*
1241 **40**:4457–4468. doi:10.1523/JNEUROSCI.0163-20.2020

1242 Smith ET, Sun P, Yu SK, Raible DW, Nicolson T. 2023. Differential expression of

1243 mechanotransduction complex genes in auditory/vestibular hair cells in zebrafish. *Front*
1244 *Mol Neurosci* **16**:1274822. doi:10.3389/fnmol.2023.1274822

1245 Söllner C, Rauch G-J, Siemens J, Geisler R, Schuster SC, the Tübingen 2000 Screen
1246 Consortium, Müller U, Nicolson T. 2004. Mutations in cadherin 23 affect tip links in
1247 zebrafish sensory hair cells. *Nature* **428**:955–959. doi:10.1038/nature02484

1248 Sotomayor M, Weihofen WA, Gaudet R, Corey DP. 2012. Structure of a force-conveying
1249 cadherin bond essential for inner-ear mechanotransduction. *Nature* **492**:128–32.
1250 doi:10.1038/nature11590

1251 Sukharev S, Corey DP. 2004. Mechanosensitive channels: multiplicity of families and gating
1252 paradigms. *Sci STKE* **2004**:re4. doi:10.1126/stke.2192004re4

1253 Tunyasuvunakool K, Adler J, Wu Z, Green T, Zielinski M, Žídek A, Bridgland A, Cowie A,
1254 Meyer C, Laydon A, Velankar S, Kleywegt GJ, Bateman A, Evans R, Pritzel A, Figurnov
1255 M, Ronneberger O, Bates R, Kohl SAA, Potapenko A, Ballard AJ, Romera-Paredes B,
1256 Nikolov S, Jain R, Clancy E, Reiman D, Petersen S, Senior AW, Kavukcuoglu K, Birney E,
1257 Kohli P, Jumper J, Hassabis D. 2021. Highly accurate protein structure prediction for the
1258 human proteome. *Nature* 1–9. doi:10.1038/s41586-021-03828-1

1259 Vallone R, Dal Cortivo G, D'Onofrio M, Dell'Orco D. 2018. Preferential Binding of Mg2+ Over
1260 Ca2+ to CIB2 Triggers an Allosteric Switch Impaired in Usher Syndrome Type 1J. *Front*
1261 *Mol Neurosci* **11**. doi:10.3389/fnmol.2018.00274

1262 Vanommeslaeghe K, MacKerell AD. 2015. CHARMM additive and polarizable force fields for
1263 biophysics and computer-aided drug design. *Biochim Biophys Acta* **1850**:861–871.
1264 doi:10.1016/j.bbagen.2014.08.004

1265 Varshney GK, Carrington B, Pei W, Bishop K, Chen Z, Fan C, Xu L, Jones M, LaFave MC,
1266 Ledin J, Sood R, Burgess SM. 2016. A high-throughput functional genomics workflow
1267 based on CRISPR/Cas9-mediated targeted mutagenesis in zebrafish. *Nat Protoc* **11**:2357–
1268 2375. doi:10.1038/nprot.2016.141

1269 Walujkar S, Lotthammer JM, Nisler CR, Sudar JC, Ballesteros A, Sotomayor M. 2021. In Silico
1270 Electrophysiology of Inner-Ear Mechanotransduction Channel TMC1 Models. *bioRxiv*
1271 2021.09.17.460860. doi:10.1101/2021.09.17.460860

1272 Wang X, Liu S, Cheng Q, Qu C, Ren R, Du H, Li N, Yan K, Wang Y, Xiong W, Xu Z. 2023.
1273 CIB2 and CIB3 regulate stereocilia maintenance and mechanoelectrical transduction in
1274 mouse vestibular hair cells. *J Neurosci*. doi:10.1523/JNEUROSCI.1807-22.2023

1275 Wang Y, Li J, Yao X, Li W, Du H, Tang M, Xiong W, Chai R, Xu Z. 2017. Loss of CIB2 causes
1276 profound hearing loss and abolishes mechanoelectrical transduction in mice. *Front Mol*
1277 *Neurosci* **10**. doi:10.3389/fnmol.2017.00401

1278 Waterhouse AM, Procter JB, Martin DMA, Clamp M, Barton GJ. 2009. Jalview Version 2--a
1279 multiple sequence alignment editor and analysis workbench. *Bioinformatics* **25**:1189–1191.
1280 doi:10.1093/bioinformatics/btp033

1281 Xiong W, Grillet N, Elledge HM, Wagner TFJ, Zhao B, Johnson KR, Kazmierczak P, Müller U.
1282 2012. TMHS is an integral component of the mechanotransduction machinery of cochlear
1283 hair cells. *Cell* **151**:1283–95. doi:10.1016/j.cell.2012.10.041

1284 Zhang M, Wang D, Kang Y, Wu J-X, Yao F, Pan C, Yan Z, Song C, Chen L. 2018. Structure of
1285 the mechanosensitive OSCA channels. *Nat Struct Mol Biol* **25**:850–858.
1286 doi:10.1038/s41594-018-0117-6

1287 Zhang Q, Li S, Wong HTC, He XJ, Beirl A, Petralia RS, Wang YX, Kindt KS. 2018.
1288 Synaptically silent sensory hair cells in zebrafish are recruited after damage. *Nat Commun*
1289 **9**:1–16. doi:10.1038/s41467-018-03806-8

1290 Zhao H, Williams DE, Shin J-B, Brügger B, Gillespie PG. 2012. Large membrane domains in
1291 hair bundles specify spatially constricted radixin activation. *J Neurosci* **32**:4600–9.
1292 doi:10.1523/JNEUROSCI.6184-11.2012

1293 Zhu S, Chen Z, Wang H, McDermott BM. 2021. Tmc Reliance Is Biased by the Hair Cell
1294 Subtype and Position Within the Ear. *Front Cell Dev Biol* **8**:570486.
1295 doi:10.3389/fcell.2020.570486

1296

1297

1298 **Figures and figure legends**

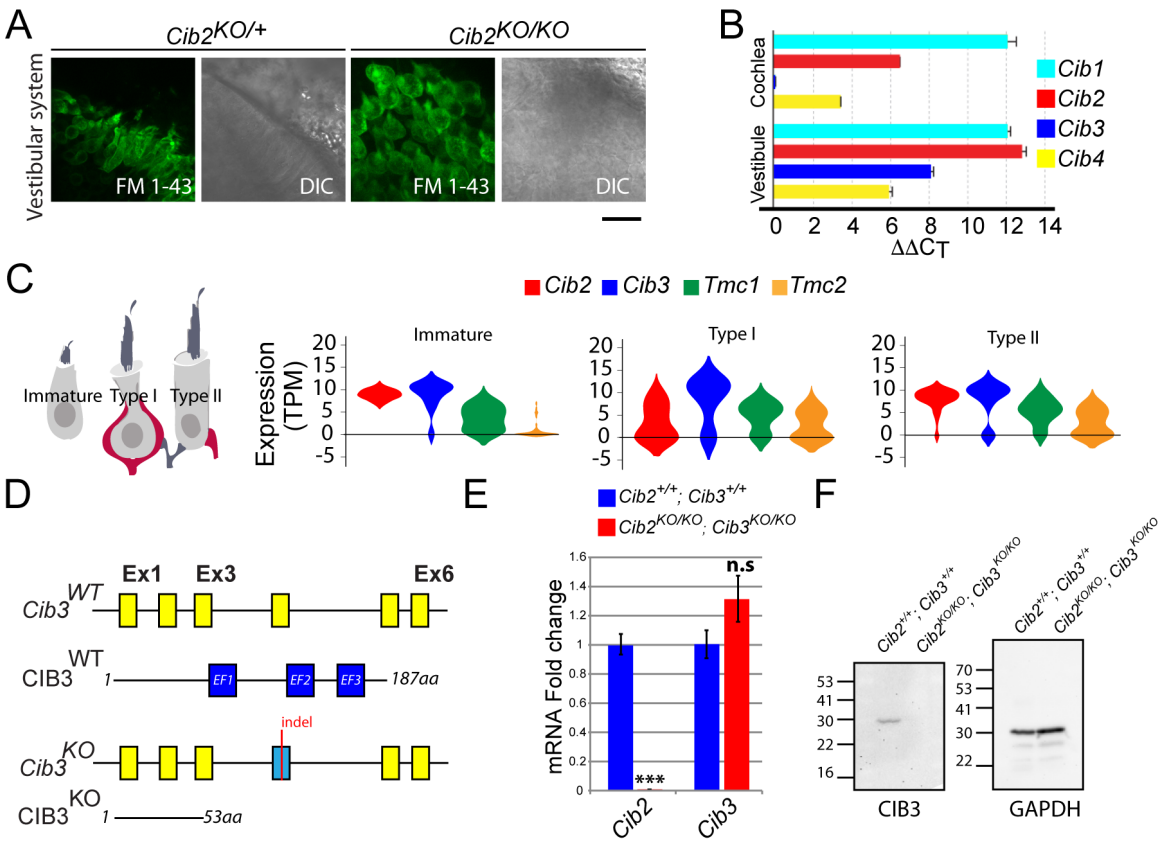

1299

1300 **Figure 1. Expression of *Cib* genes in the mouse inner ear and generation of *Cib3* knockout**

1301 **mice.** (**A**) Maximum intensity projections of Z-stacks of confocal fluorescent images and

1302 corresponding DIC images of $Cib2^{KO/+}$ and $Cib2^{KO/KO}$ cultured vestibular end organ explants

1303 imaged after exposure to 3 µM of FM 1-43 for 10 s. The samples were dissected at P5 and kept 2

1304 days *in vitro* (P5 + 2div). Scale bar: 20 µm. (**B**) Real-time quantitative RT–PCR analysis of mRNA

1305 levels in the cochlear and vestibular sensory epithelia at P12 revealed different expression of *Cib1*,

1306 *Cib2*, *Cib3,* and *Cib4* in the auditory and vestibular end organs. (**C**) Violin plots generated by

1307 gEAR portal showing the expression levels of *Cib2*, *Cib3*, *Tmc1,* and *Tmc2* by scRNA-seq in

1308 immature, type 1, and type 2 utricular vestibular hair cells. TPM: transcript per million. (**D**) Gene

1309 structure of the wild-type and *Cib3*^{KO} alleles. Exons are shown in yellow. Indel in exon 4 leads to
1310 a nonsense mutation and a premature stop at the protein level (p. Asp54*) (**E**) Real-time
1311 quantitative RT–PCR analysis using cDNA from brain tissue of *Cib2;Cib3* mutant mice was used
1312 to analyze the expression of *Cib2* and *Cib3*. Contrary to *Cib2* mRNA, *Cib3* mRNA appears to be
1313 stable in the *Cib2*$^{KO/KO}$*;Cib3*$^{KO/KO}$ mice and does not go through nonsense mediated decay process.
1314 The relative expression of *Cib2* and *Cib3* members were normalized against *hprt*. Asterisks
1315 indicate statistical significance: ***, $p<0.001$ (Student's t-test). n.s.: not significant. Error bars
1316 represent SEM. (**F**) Western Blot analysis on *Cib2;Cib3* mouse heart tissue was performed
1317 using CIB3 antibody. No CIB3 protein was detected in the *Cib2*$^{KO/KO}$*;Cib3*$^{KO/KO}$ mice, validating
1318 our mouse model. GAPDH detection was used as a loading control.
1319
1320

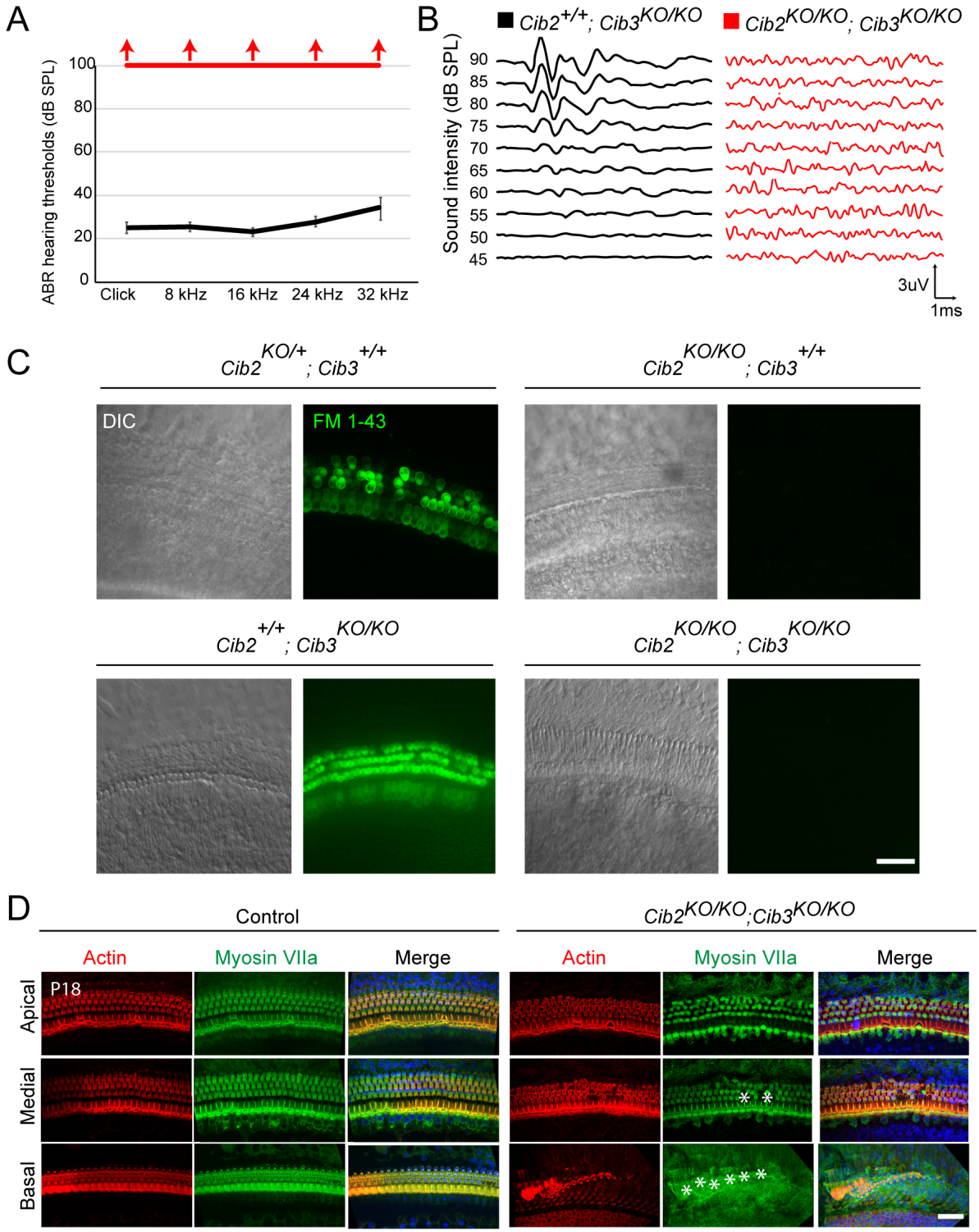

1321

1322 **Figure 2. CIB2/3 double mutant mice have profound hearing loss.** (**A**) ABR thresholds to

1323 broadband clicks and tone-pips with frequencies of 8 kHz, 16 kHz, 24 kHz and 32 kHz in
1324 *Cib2*$^{+/+}$;*Cib3*$^{KO/KO}$ (black; n = 5) and *Cib2*$^{KO/KO}$;*Cib3*$^{KO/KO}$ (red, n = 5) mice at P16. The same
1325 animals were tested with clicks and tone pips. (**B**) ABR pure tone traces of P32 *Cib2*$^{+/+}$;*Cib3*$^{KO/KO}$
1326 (black) and *Cib2*$^{KO/KO}$;*Cib3*$^{KO/KO}$ (red) mice measured at 32 kHz. Hearing thresholds are in
1327 Decibels (dB SPL). (**C**) Maximum intensity projections of Z-stacks of confocal fluorescent images
1328 (right) and corresponding DIC images (left) of *Cib2*$^{KO/+}$;*Cib3*$^{+/+}$, *Cib2*$^{KO/KO}$;*Cib3*$^{+/+}$,
1329 *Cib2*$^{+/+}$;*Cib3*$^{KO/KO}$ and *Cib2*$^{KO/KO}$;*Cib3*$^{KO/KO}$ cultured organ of Corti explants imaged after
1330 exposure to 3 µM of FM 1-43 for 10 s. The samples were dissected at P5 and kept 2 days in vitro
1331 (P5 + 2div). Scale bar: 20 µm. (**D**) Maximum intensity projections of confocal Z-stacks of apical,
1332 medial and basal turns of organ of Corti of control and *Cib2*$^{KO/KO}$;*Cib3*$^{KO/KO}$ mice immunostained
1333 with an anti-myosin VIIa antibody (green) and counterstained with phalloidin (red) at P18.
1334 Asterisks indicate hair cell loss. Scale bar: 10 µm.
1335
1336

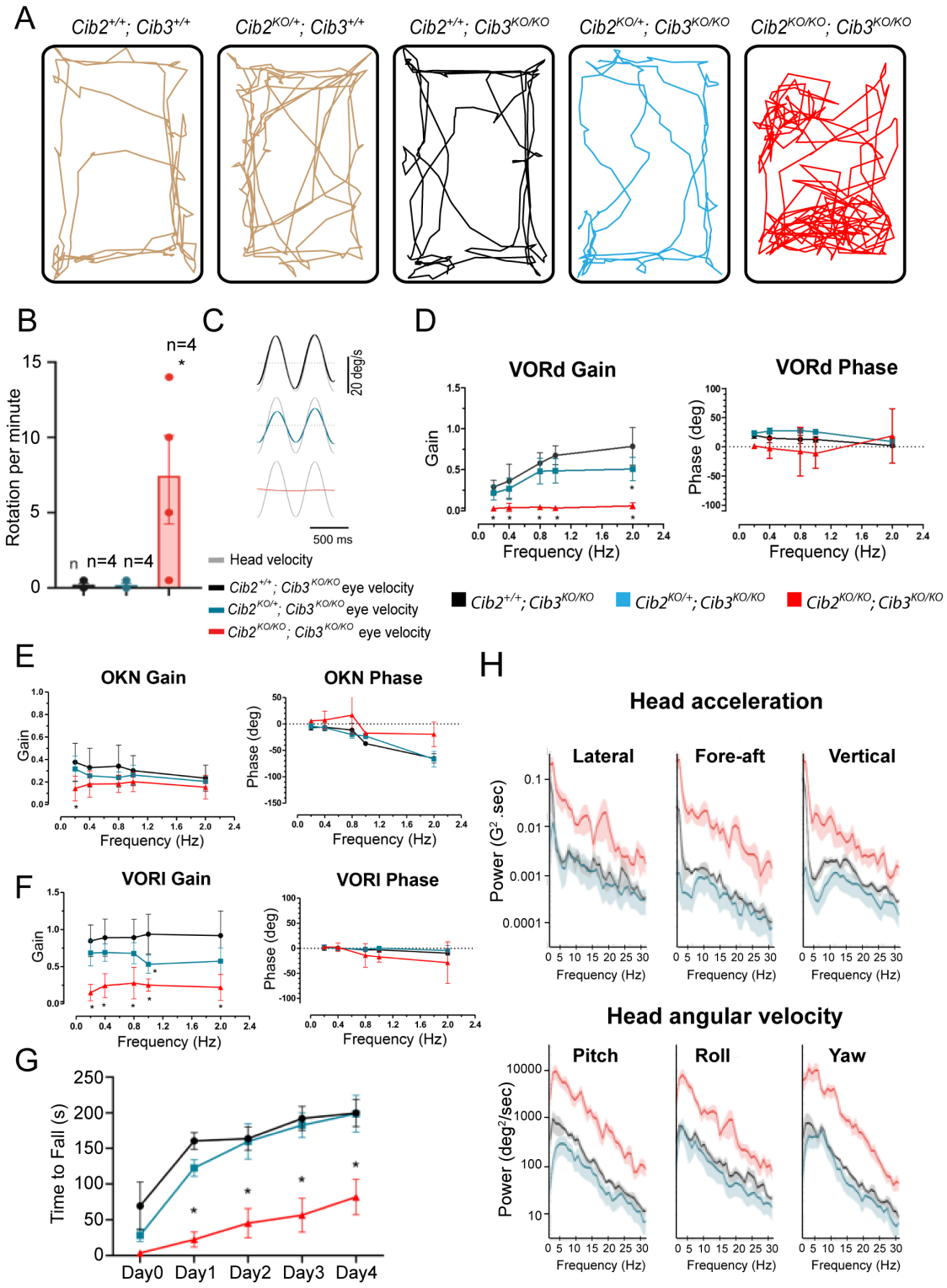

Figure 3. CIB2/3 double mutant mice have vestibular dysfunction. (**A**) Traces showing the open-field exploratory behavior of P60 *Cib2*$^{+/+}$;*Cib3*$^{+/+}$, *Cib2*$^{KO/+}$;*Cib3*$^{+/+}$, *Cib2*$^{+/+}$;*Cib3*$^{KO/KO}$,

1340 *Cib2*$^{KO/+}$;*Cib3*$^{KO/KO}$ and *Cib2*$^{KO/KO}$;*Cib3*$^{KO/KO}$ mutant mice. (**B**) Quantification of the number of
1341 rotations in 120 seconds (mean ± SEM), showing that, unlike *Cib2*$^{+/+}$;*Cib3*$^{KO/KO}$, and
1342 *Cib2*$^{KO/+}$;*Cib3*$^{KO/KO}$ mice, *Cib2*$^{KO/KO}$;*Cib3*$^{KO/KO}$ mutant mice display a circling behavior and a
1343 vestibular defect (*t*-test) (n = 4 for each genotype). (**C**) Examples of head-velocity (grey) and
1344 resultant eye-velocity traces evoked during VORd testing. Note, the eye movement is
1345 compensatory, and the trace has been inverted to facilitate comparison with head velocity. (**D**)
1346 VORd Gain and phase (mean ± SD) plotted as a function of frequency for *Cib2*$^{+/+}$;*Cib3*$^{KO/KO}$ (n =
1347 4), *Cib2*$^{KO/+}$;*Cib3*$^{KO/KO}$ (n = 5), *Cib2*$^{KO/KO}$;*Cib3*$^{KO/KO}$ (n = 4). (**E**) OKN gain and phase (mean ±
1348 SD) plotted as a function of frequency for *Cib2*$^{+/+}$; *Cib3*$^{KO/KO}$ (n = 4), *Cib2*$^{KO/+}$;*Cib3*$^{KO/KO}$ (n = 5),
1349 *Cib2*$^{KO/KO}$;*Cib3*$^{KO/KO}$ (n = 4). (**F**) VORl gain and phase (mean ± SD) plotted as a function of
1350 frequency for *Cib2*$^{+/+}$;*Cib3*$^{KO/KO}$ (n = 4), *Cib2*$^{KO/+}$;*Cib3*$^{KO/KO}$ (n = 5), *Cib2*$^{KO/KO}$;*Cib3*$^{KO/KO}$ (n = 4).
1351 Comparisons made with two-way ANOVA followed by Bonferroni post-hoc test for (A-D); *$p <$
1352 0.05. (**G**) Quantification of the time mice remained on the rotating rod with increasing acceleration
1353 (mean ± SEM). Comparisons made with two-way ANOVA followed by Bonferroni post-hoc test
1354 for (F-K); *P<0.002. (*Cib2*$^{+/+}$;*Cib3*$^{KO/KO}$ (n = 6), *Cib2*$^{KO/+}$;*Cib3*$^{KO/KO}$ (n = 6), *Cib2*$^{KO/KO}$;*Cib3*$^{KO/KO}$
1355 (n = 6)). (**H**) Comparison of power spectra density of head movements in translational axes (top)
1356 and rotational axes (bottom) between wild type (*Cib2*$^{+/+}$;*Cib3*$^{KO/KO}$, black), heterozygous mutants
1357 (*Cib2*$^{KO/+}$;*Cib3*$^{KO/KO}$, blue), and homozygous mutants (*Cib2*$^{KO/KO}$;*Cib3*$^{KO/KO}$, red). The double
1358 knockout *Cib2*$^{KO/KO}$;*Cib3*$^{KO/KO}$ exhibit significantly higher power than *Cib2*$^{+/+}$;*Cib3*$^{KO/KO}$ and
1359 *Cib2*$^{KO/+}$;*Cib3*$^{KO/KO}$ across all frequencies (0–30 Hz), in all six translational and rotational axes.
1360

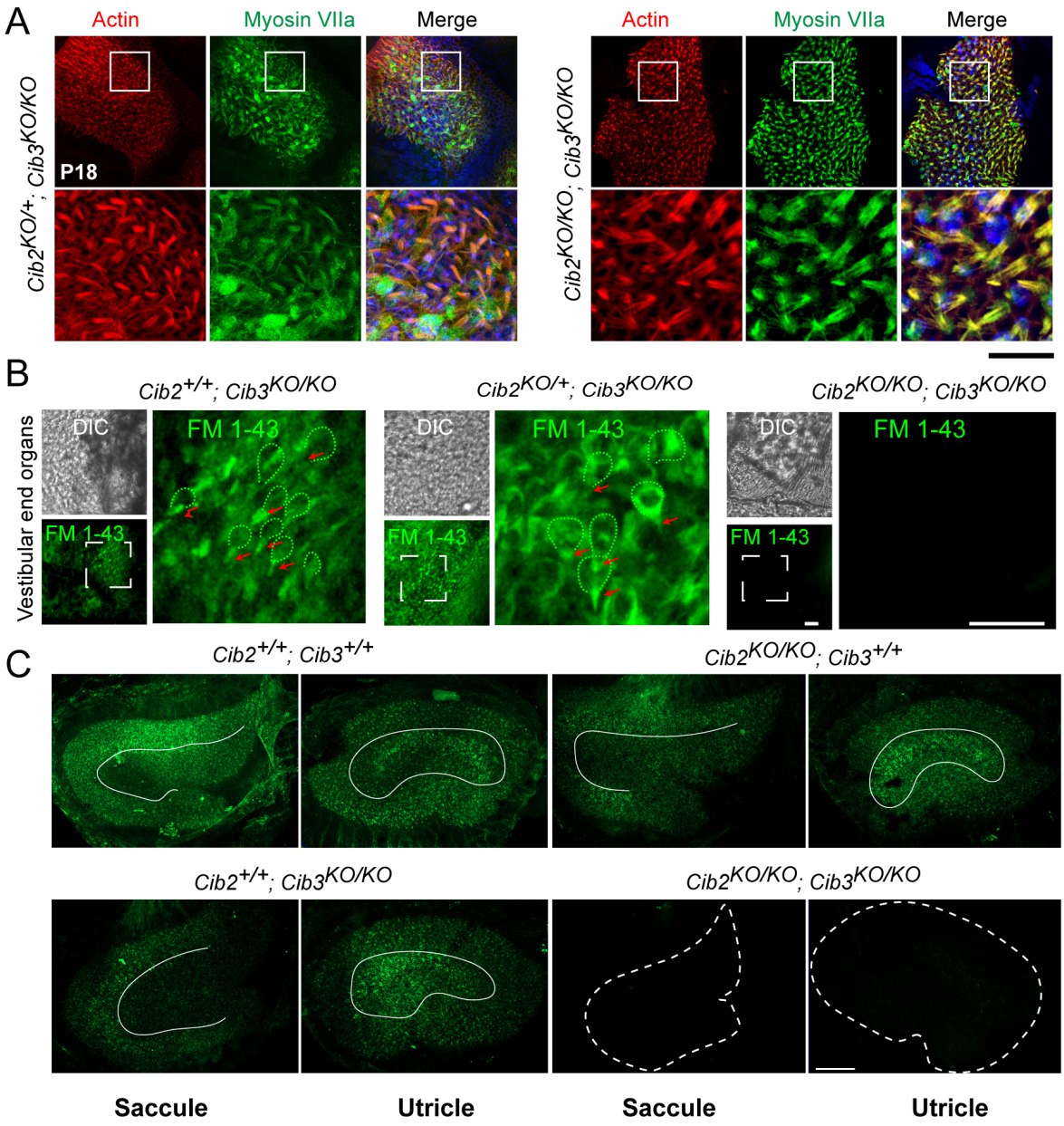

1361

1362 **Figure 4. Vestibular hair cells do not have functional MET channels at rest in CIB2/3 double**
1363 **mutant mice.** (**A**) Maximum intensity projections of confocal Z-stacks of the vestibular end
1364 organs of P18 *Cib2*$^{KO/+}$;*Cib3*$^{KO/KO}$ and *Cib2*$^{KO/KO}$;*Cib3*$^{KO/KO}$ mutant mice immunostained with
1365 myosin VIIa antibody (green) and counterstained with phalloidin (red) and DAPI (blue). Scale bar
1366 = 50 µm. (**B**) Adult vestibular end organs of *Cib2*$^{+/+}$;*Cib3*$^{KO/KO}$, *Cib2*$^{KO/+}$;*Cib3*$^{KO/KO}$ and

1367 *Cib2*$^{KO/KO}$;*Cib3*$^{KO/KO}$ mutant mice imaged after exposure to 3 μM of FM 1-43 for 10 s. Vestibular
1368 hair cell bodies (green doted lines), and stereocilia bundles (red arrows) are shown. Scale bar:
1369 100 μm. (**C**) FM 1-43FX (fixable form) labeling of saccules and utricles by IP injection at P60.
1370 Obvious reduction in signal in *Cib2*$^{KO/KO}$;*Cib3*$^{KO/KO}$, and subtle extrastriolar reduction in
1371 *Cib2*$^{+/+}$;*Cib3*$^{KO/KO}$ mice was observed. Extrastriolar regions are delimited with white lines. Scale
1372 bar = 100 μm.
1373
1374

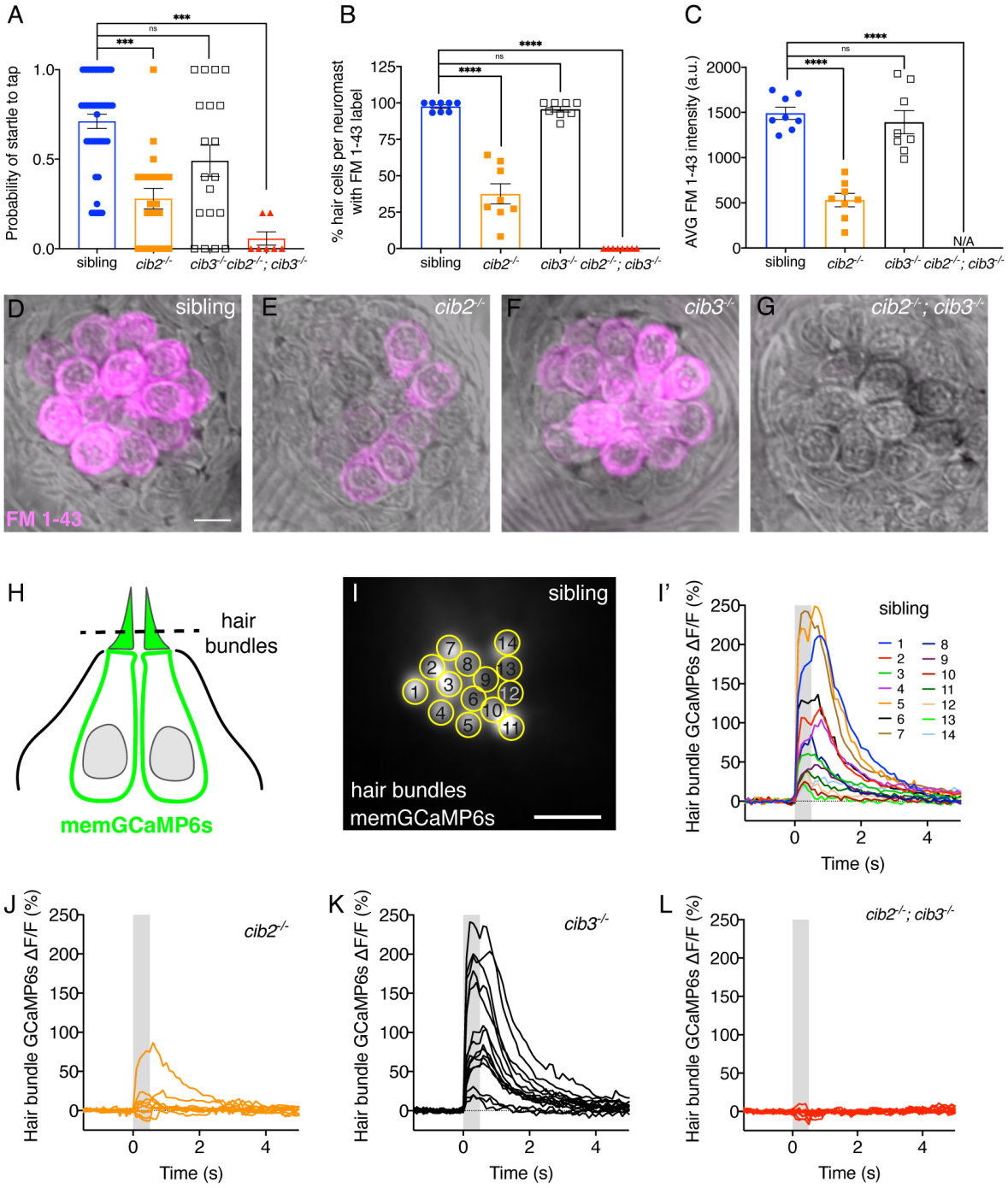

1375

1376 **Figure 5. Both Cib2 and Cib3 are required in zebrafish for acoustic startle and MET**

1377 **function.** (**A**) Compared to controls (siblings) *cib3* mutants have a normal acoustic startle

1378 response. *Cib2;cib3* double mutants completely lack an acoustic startle response, while *cib2*

1379 mutants have a reduced probability to startle compared to controls (*n* = 43 sibling, 20 *cib2*, 19 *cib3*
1380 and 7 *cib2;cib3* animals). (**B**) Compared to controls *cib3* mutants have a normal % of hair cells
1381 that label with FM 1-43 per neuromast. In *cib2;cib3* mutants no hair cells label with FM 1-43, and
1382 in *cib2* mutants a significantly reduced % of hair cells label with FM 1-43 per neuromast. (**C**) The
1383 average intensity of FM 1-43 labeling in *cib3* mutant hair cells is similar to controls. In contrast,
1384 in *cib2* mutants, hair cells that label with FM 1-43, have a significantly reduced intensity compared
1385 to controls (*n* = 8 neuromasts per genotype in B and C). (**D-G**) Representative neuromasts labeled
1386 with FM 1-43 for each genotype. FM 1-43 label is overlaid onto laser scanning DIC images. (**H**)
1387 Schematic showing the localization of membrane-localized GCaMP6s (memGCaMP6s); the
1388 indicator used to measure Ca^{2+} influx into lateral-line hair bundles. The plane used for Ca^{2+}
1389 imaging and to determine if a hair cell is mechanosensitive is indicated by the dashed line. (**I-I'**)
1390 Representative example of a hair bundle imaging plane (I), along with the resulting Ca^{2+} responses
1391 (I') from hair bundles from a control neuromast. The ROIs used to measure Ca^{2+} signals in each
1392 hair bundle are indicated in (I). (**J-L**) Representative examples of Ca^{2+} responses from neuromasts
1393 in *cib2* (J), *cib3* (K) and *cib2;cib3* mutants (L). FM 1-43 imaging and behavior were performed at
1394 5 dpf. Ca^{2+} imaging was performed at 5 or 6 dpf. A Kruskal-Wallis test was used in A; A one-way
1395 ANOVA was used in B and C. The scale bar in D and I = 5 μm. The online version of this article
1396 includes source data and the following figure supplement(s) for Figure 5.
1397
1398 The online version of this article includes source data and the following figure supplement(s) for
1399 Figure 5.
1400 **Figure supplement 1.** Summary of zebrafish *cib2* and *cib3* alleles used in this study.
1401 **Figure supplement 2.** Summary of mechanosensitive Ca^{2+} responses in zebrafish.

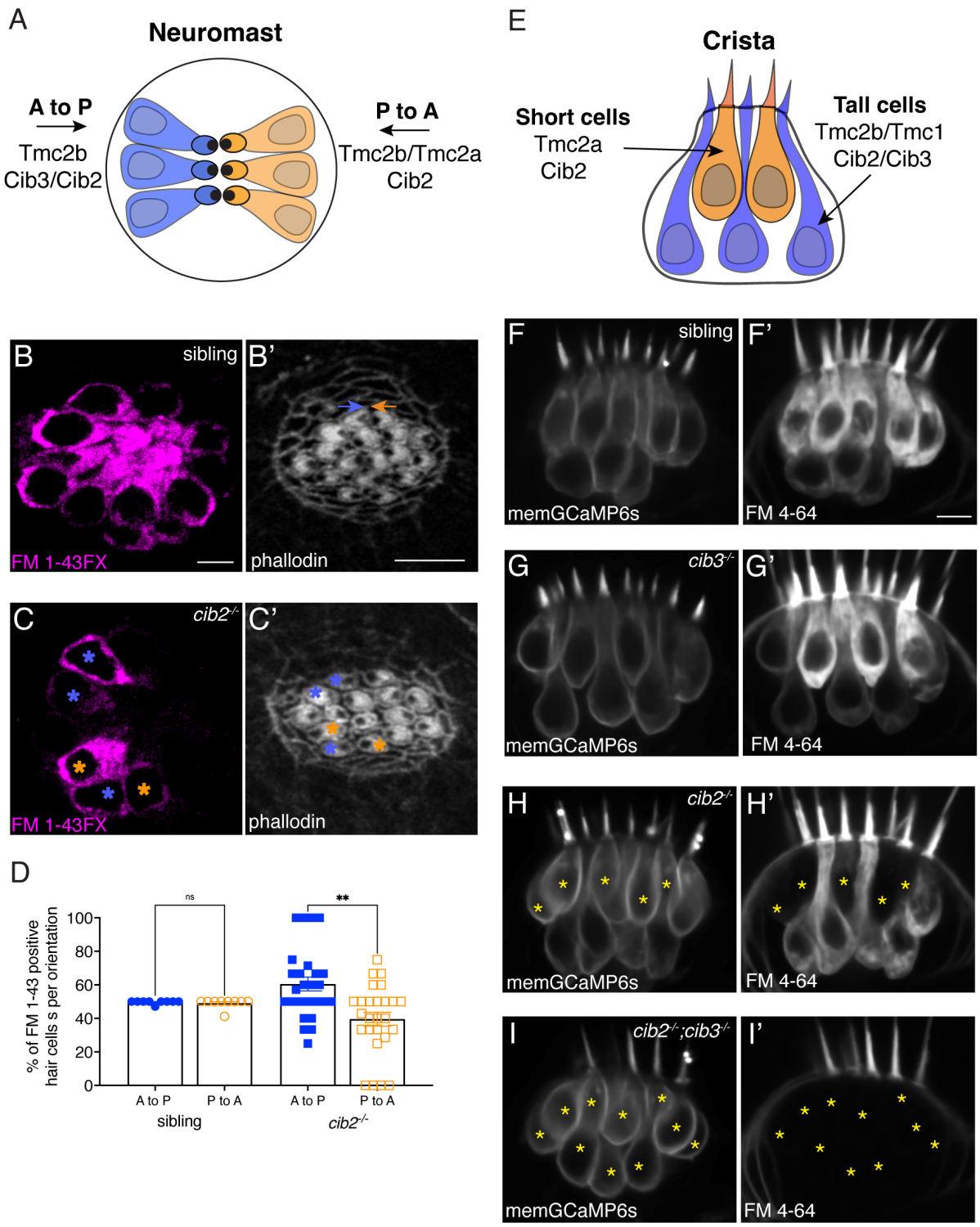

Figure 6. Cib2 is required in specific subsets of hair cells in the zebrafish pLL and inner ear. (**A**) Overview of Tmc requirements in pLL hair cells. Hair cells that sense posterior flow (orange)

1405 rely on Tmc2b, while hair cells that sense anterior flow (blue) can rely on Tmc2b and/or Tmc2a
1406 for mechanosensitive function. (**B-C'**) FM 1-43FX labeling in pLL neuromasts from sibling
1407 control (B) and *cib2* mutants (C). The residual cells in *cib2* mutants rely on Cib3 for
1408 mechanosensitive function. Phalloidin label can be used to link FM 1-43FX label to the orientation
1409 of pLL hair cells (C,C'; see colored asterisks). In B', orange and blue arrows rest above hair cells
1410 that are oriented to respond to anterior and posterior flow, respectively. (**D**) Quantification reveals
1411 that a similar percentage of anterior and posterior responsive pLL hair cells label with FM 1-43FX
1412 in sibling controls (posterior flow: 49.7 %, anterior flow: 49.2 %, n = 9 neuromasts). In contrast,
1413 in *cib2* mutants, a significantly higher percentage of posterior responsive pLL hair cells label with
1414 FM 1-43FX in *cib2* mutants (posterior flow: 60.5 %, anterior flow: 39.5 %, n = 26 neuromasts).
1415 (**E**) Overview of Tmc and Cib requirements in the hair cells of zebrafish cristae. Short teardrop-
1416 shaped cells rely primarily on Tmc2a, while tall gourd-shaped cells rely primarily on Tmc2b and
1417 Tmc1. (**F-I'**) Medial cristae for each genotype. MemGCaMP6s labels all hair cells, while FM 4-
1418 64 labels hair cells with intact mechanosensitive function. In siblings and *cib3* mutants, both
1419 teardrop and gourd cells label with FM 4-64 (F-F', G-G'). In *cib2;cib3* double mutants, no hair
1420 cells label with FM 4-64 (asterisks) (I-I'). In *cib2* mutants many short cells fail to label with FM
1421 4-64 (asterisks) (H-H'), (n = 13 double het sibling, 7 *cib3*, 14 *cib2* and 4 double mutant crista). All
1422 images were acquired at 5 dpf. A Kruskal-Wallis test was used in D; $P > 0.01$. The scale bars in
1423 B, B', and F' = 5 µm.
1424
1425

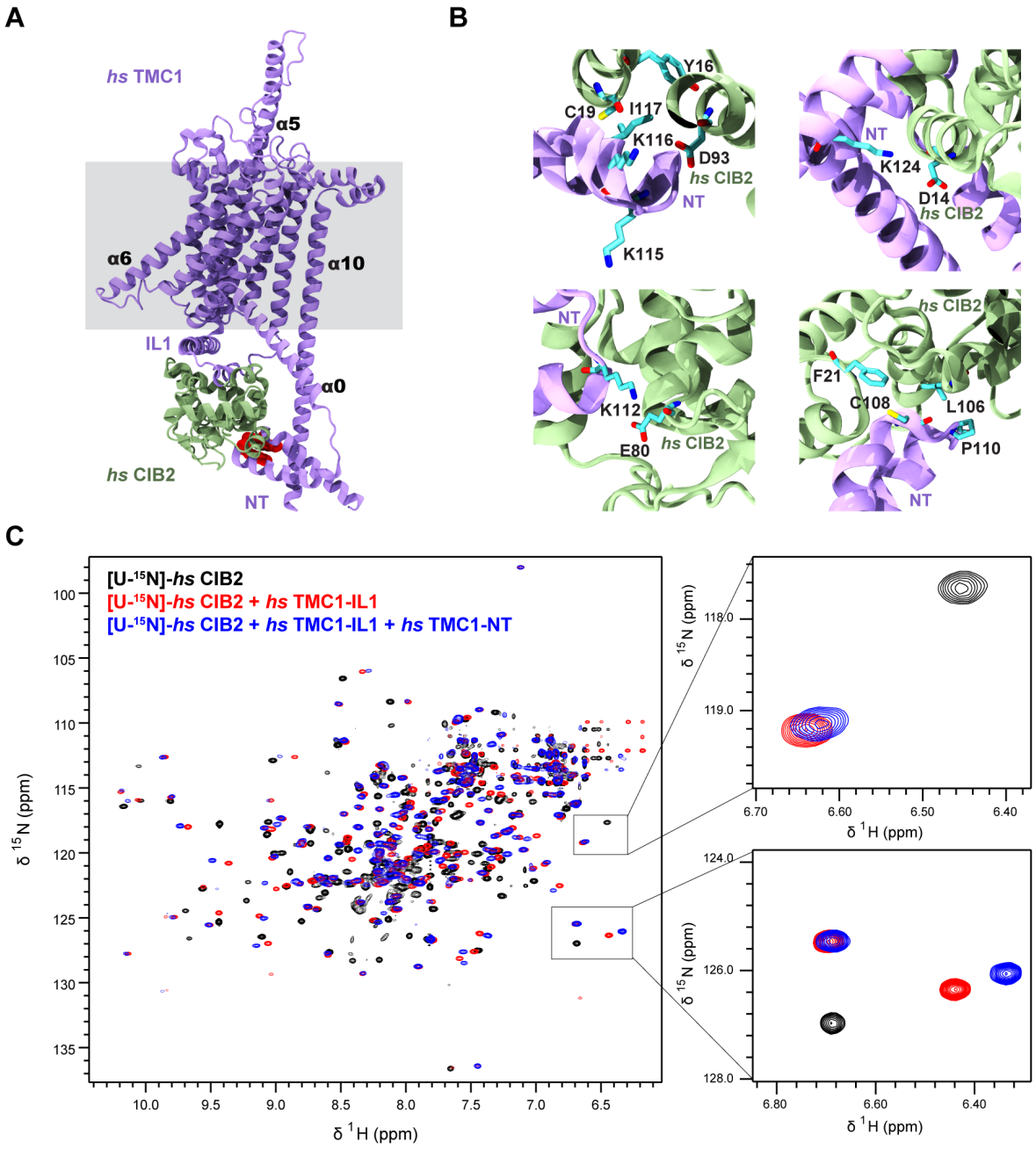

1426

1427 **Figure 7. AF2 predictions and NMR data support a clamp-like model for the human TMC1**

1428 **and CIB2 complex**. (**A**) AF2 model of *hs* TMC1 in complex with *hs* CIB2. Side view of

1429 monomeric *hs* TMC1 (light purple) in complex with *hs* CIB2 (light sea green). N-terminal residues

1430 of TMC1 known to interact with CIB2 are in red. (**B**) Top left panel shows residues at the *hs*

1431 TMC1-NT fragment (115-117) shown to weaken interaction with CIB2 upon mutation (Liang et
1432 al., 2021) at the interface with CIB2. Additional panels show details of contacts between TMC1
1433 and CIB2 with formation of K124:D14 and K112:E80 salt bridges, as well as hydrophobic
1434 interactions. (**C**) Overlay of ^{1}H-^{15}N TROSY-HSQC spectra of *hs* [U-^{15}N]-CIB2 (black) alone and
1435 bound to either only *hs* TMC1-IL (red) or both *hs* TMC1-IL and *hs* TMC1-NT (blue). NMR data
1436 were obtained in the presence of 3 mM $CaCl_2$. These data are also shown in Figure 7-figure
1437 supplement 7.
1438
1439 The online version of this article includes source data and the following figure supplement(s) for
1440 Figure 7.
1441 **Figure supplement 1.** Overview of TMC1/2 and CIB2/3 AF2 models.
1442 **Figure supplement 2.** TMC sequence alignment.
1443 **Figure supplement 3.** CIB2 sequence alignment.
1444 **Figure supplement 4.** CIB3 sequence alignment.
1445 **Figure supplement 5.** CIB sequence alignment.
1446 **Figure supplement 6.** SEC of *hs* CIB2 and *hs* CIB3 either refolded alone or co-refolded with *hs* TMC1-
1447 IL1, and *hs* TMC1-NT.
1448 **Figure supplement 7.** ^{1}H-^{15}N TROSY-HSQC spectra.
1449 **Figure 7–video 1.** Overview of *hs* TMC1 (light and dark purple) in complex with *hs* CIB2 (light
1450 sea green)-Ca^{2+} (green spheres). K^{+} ions (pink) were shown to be permeating the pore region
1451 between α4 and α6. Water molecules, lipids, and protein side chains were omitted for clarity.
1452

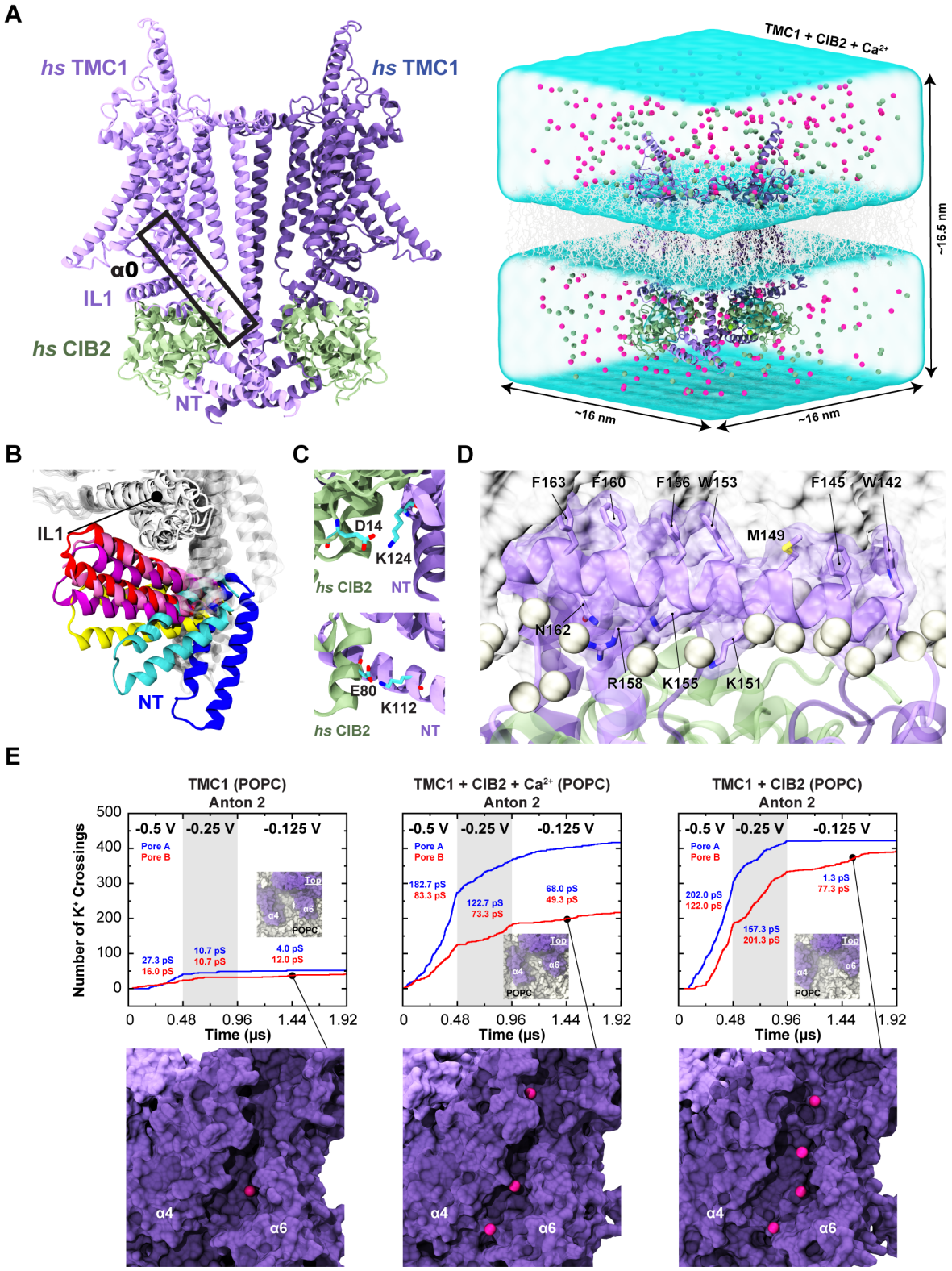
A
hs TMC1
hs TMC1
α0
IL1
hs CIB2
NT
TMC1 + CIB2 + Ca2+
~16.5 nm
~16 nm
~16 nm
B
IL1
NT
C
D14
K124
hs CIB2
NT
E80
K112
hs CIB2
NT
D
F163
F160
F156
W153
F145
W142
M149
N162
R158
K155
K151
E
TMC1 (POPC)
Anton 2
TMC1 + CIB2 + Ca2+ (POPC)
Anton 2
TMC1 + CIB2 (POPC)
Anton 2
Number of K+ Crossings
Time (μs)
-0.5 V
-0.25 V
-0.125 V
Pore A
Pore B
27.3 pS
16.0 pS
10.7 pS
10.7 pS
4.0 pS
12.0 pS
182.7 pS
83.3 pS
122.7 pS
73.3 pS
68.0 pS
49.3 pS
202.0 pS
122.0 pS
157.3 pS
201.3 pS
1.3 pS
77.3 pS
Top
α4
α6
POPC

1453

1454 **Figure 8. Simulations of AF2 predictions show that human TMC1 and CIB2 complexes form**
1455 **cation channels**.
1456 (**A**) *Left:* AF2 model of the dimeric *hs* TMC1 + *hs* CIB2 complex. *Right:* A complete simulation
1457 system of *hs* TMC1 in complex with *hs* CIB2-Ca^{2+} is shown in surface representation. *hs* TMC1
1458 is shown in light (monomer A) and dark (monomer B) purple, *hs* CIB2 in light sea green, water in
1459 transparent light blue, lipid membrane in gray lines, and K^+ and Cl^- ions are shown as pink and
1460 green spheres, respectively. (**B**) The *hs* TMC1-NT domain explores diverse conformational space
1461 in the absence of CIB during equilibrium simulations (S3a). (**C**) Salt bridges K124:D14 and
1462 K112:E80 remain throughout equilibrium simulations. (**D**) Snapshot of amphipathic helix α0
1463 inserting into the lipid bilayer (S4c). (**E**) Number of K^+ crossings as a function of time for pores
1464 A and B of *hs* TMC1, *hs* TMC1 + *hs* CIB2 + Ca^{2+}, and *hs* TMC1 + *hs* CIB2 in a POPC bilayer at
1465 -0.5 V, -0.25 V, and -0.125 V. Insets show top views of pore region with TMC1 (dark purple) and
1466 lipids (light gray) in surface representation (protein and lipids partially excluded for clarity).
1467 Representative images of K^+ permeating the pore region between α4 and α6 of *hs* TMC1 are shown
1468 with protein in surface representation and ions as pink spheres. Conductance values calculated for
1469 K^+ crossings.
1470
1471 The online version of this article includes source data and the following figure supplement(s) for
1472 Figure 8.
1473 **Figure supplement 1.** Stability of TMC/CIB complexes, monomers, and subdomains.
1474 **Figure supplement 2.** BSA in *hs* TMC1/2 and *hs* CIB2/3 complexes.
1475 **Figure supplement 3.** Number of K^+ crossings as a function of time for pores A and B of *hs* TMC1 and
1476 *hs* TMC2.

1477 **Figure supplement 4.** Conduction events in long timescale simulations and summary of predicted
1478 conductance values.

1479 **Figure supplement 5.** Possible combinations of TMC1, TMC2, CIB2, and CIB3 complexes.

1480 **Figure 8–video 1.** Side view of the *hs* TMC1 channel pore during a trajectory at -0.5 V (monomer
1481 B). K^+ (pink) are seen permeating the pore from one side (S1b); *hs* TMC1 (monomer B) is shown
1482 in dark purple and *hs* CIB2 is shown in light sea green. Water molecules, lipids, *hs* TMC1
1483 (monomer A), and protein side chains were omitted for clarity.
1484
1485 **Figure 8–table supplement 1.** Summary of simulations.
1486
1487 **Figure 8–table supplement 2.** Ion conduction.
1488

1489